Geophys. J. Int. (2009) doi: 10.1111/j.1365-246X.2009.04242.x

Mantle reflectivity structure beneath oceanic hotspots

Yu Jeffrey Gu,[1] Yuling An,[1] Mauricio Sacchi,[1] Ryan Schultz[1] and Jeroen Ritsema[2]

[1]*Department of Physics, University of Alberta, Edmonton,* AB T6G 2G7, *Canada. E-mail: jgu@phys.ualberta.ca*
[2]*Department of Geological Sciences, University of Michigan, Ann Arbor,* MI 48109, *USA*

Accepted 2009 May 6. Received 2009 May 4; in original form 2008 November 30

SUMMARY

This study applies high-resolution Radon transform to a large set of *SS* precursors and explores the mantle reflectivity structure beneath 17 potentially 'deep-rooted' hotspots. The combined reduced time (τ) and ray parameter (p) information effectively constrains the depth, spatial distribution and sharpness of upper-/mid-mantle reflectors. The olivine to wadsleyite phase boundary is deeper than the ocean and global averages and produces a dominant τ –p domain signal. Laterally coherent observations of the deep 410-km seismic discontinuity, thin upper mantle transition zone and weak/absent 520-km reflector beneath hotspots make compelling arguments for large-scale, hot thermal anomalies in the top 400–600 km of the mantle. On the other hand, a relatively 'flat' and weak reflector at ∼653 km is inconsistent with ringwoodite to silicate perovskite + magnesiowüstite transformation at temperatures greater than 2000 K. The lack of a negative correlation between topography and temperature implies (1) average or below-average temperatures at 600–700 km depths or (2) high temperatures and a dominating majorite garnet to Ca perovskite phase transformation. The proper choice between these two scenarios will directly impact the origin and depth of mantle plumes beneath hotspots. We further identify lower-mantle reflectors at 800–950 and 1100–1350 km depths beneath a number of the hotspots. Their presence implies that the chemistry and thermodynamics of the mid-mantle may be more complex than suggested by seismic tomography.

Key words: Inverse theory; Body waves; Wave scattering and diffraction; Dynamics of lithosphere and mantle; Dynamics: convection currents, and mantle plumes; Hotspots.

1 INTRODUCTION

Global characterization of melting anomalies (or 'hotspots') generally centre on two competing hypotheses: (1) the 'plume model' (Morgan 1971; Sleep 1990) that predicates on buoyancy-driven thermal anomalies originating from the deep-mantle; (2) the 'plate model' (Anderson 2001, 2005; Foulger 2007) that accentuates the role of lithosphere, plate stresses and recycling of the enriched crust. Discussions of melting anomalies received greater attention when global catalogues (e.g. Davies 1988; Sleep 1990; Steinberger *et al* 2004; Courtillot *et al.* 2003; Anderson 2005) were introduced to reconcile a wide range of reported surface expressions, mantle seismic wave speeds, heat flow and isotopic compositions pertaining to hotspots (see Nataf 2000; Foulger 2007 for detailed reviews). Among the various geophysical and geochemical constraints, seismic observations offer some of the most compelling arguments in the 'plume debate'. Pervasive evidence of hot thermal/compositional anomalies near the core–mantle boundary (CMB; e.g. Su *et al.* 1994; Grand *et al.* 1997; van der Hilst *et al.* 1997; van der Hilst & Karason 1999; Kellogg *et al.* 1999; Rost *et al.* 2005; Lay 2005) and their spatial correlation with hotspots (e.g. Ritsema *et al.* 1999; Li *et al.* 2000; Montelli *et al.* 2004; Zhao 2004) favours the plume model. On the other hand, well-documented resolution issues in seismic tomography (Romanowicz 2003; Ritsema *et al.* 2004) and the effects of continental roots (Ebinger & Sleep 1998; Sleep *et al.* 2002; Lin *et al.* 2005; Manglik & Christensen 2006) and phase transitions (Shen *et al.* 2002; Hirose 2002; Nolet *et al.* 2006) on plume ascent raise questions about the presence and vertical continuity of hot thermal anomalies.

A self-consistent explanation for the origin of globally distributed hotspots requires detailed knowledge of the speed and reflectivity in the upper mantle transition region (400–1000 km). This depth range features two major mineralogical phase changes (e.g. Ringwood 1975; Agee & Walker 1988; Anderson 1989) with a strong temperature dependence and a propensity to cause disruptions to mantle flow (e.g. Tackley *et al.* 1993; Gu *et al.* 2001; Fukao *et al.* 2001; Nolet *et al.* 2006). In theory, a vertically continuous hot plume ascending through the mantle transition zone (400–700 km, from here on, MTZ) can be identified through (1) locally reduced seismic speeds and (2) converging 410- and 660-km olivine phase boundaries (Katsura & Ito 1989; Ito & Takahashi 1989; Bina & Helffrich 1994). Orientation and strength of seismic anisotropy could provide additional constraints on dominant flow directions in and around MTZ (e.g. Trampert & van Heijst 2002; Panning & Romanowicz 2006; Zhou *et al.* 2006; Visser *et al.* 2008). In practice, the details of MTZ seismic velocities from tomographic

inversions remain sketchy on the global scale (Becker & Boschi 2002; Romanowicz 2003; Ritsema *et al.* 2004). Observations of a locally thin MTZ in support of the opposite deflections of olivine phase boundaries have also been questioned (Gilbert *et al.* 2003; Deuss 2007), even for the widely studied Iceland hotspot (Shen *et al.* 2002, 2003; Du *et al.* 2006). The existence of weak reflectors/discontinuities (e.g. Shearer 1991; Gu *et al.* 1998; Weidner & Wang 2000; Deuss & Woodhouse 2001) and velocity reversals (Vinnik & Fara 2006) within the MTZ introduces further complexities to the discussion of the origin depth and role of mantle plumes.

In this study, we present a systematic analysis of the strengths and depths of mantle discontinuities beneath hotspots based on a high-resolution Radon transform (HRT) method. The lateral and depth sensitivities provided by *SS* precursors (Fig. 1a), the primary data set of this study, are ideal for global surveys due to the use of midpoints in place of the more restrictive source or station locations. Our frequency-domain approach effectively eliminates both correlated and uncorrelated noise that could compromise the quality of common midpoint stacks. This study is partly motivated by a recently proposed hotspot criterion (Deuss 2007) that links 'deep-rooted' hotspots to a deep 410-km discontinuity and an average or thin MTZ. We target 17 hotspots that score a value of 2 or higher according to the hotspot criteria of Courtillot *et al.* (2003) and present a consistent global picture of the large-scale reflectivity structure surrounding mantle plumes. For the remainder of this study, we make the following abbreviations to improve succinctness: (1) Deuss *et al.* (2007) to Deuss07 and (2) 410-, 520- and 660-km seismic discontinuities to *410, 520* and *660*, respectively.

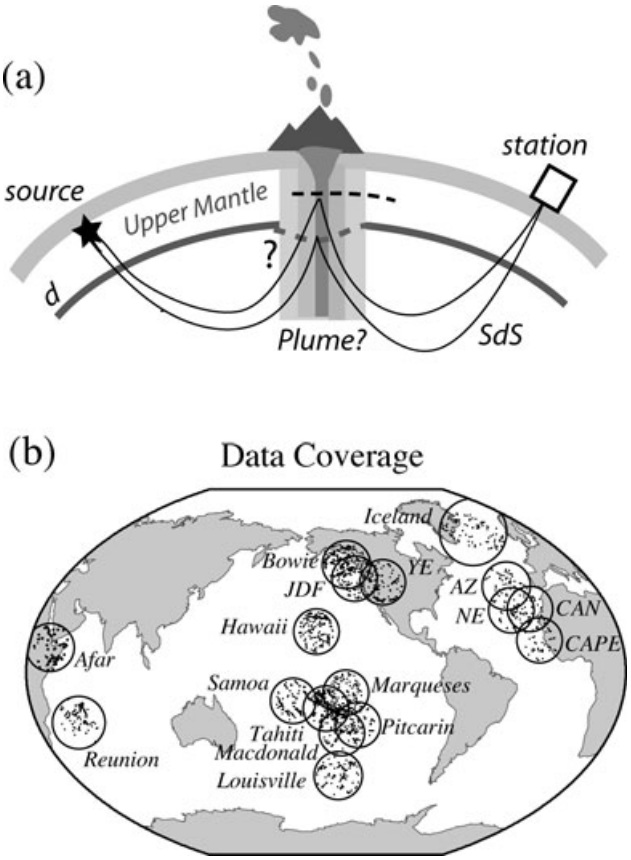

Figure 1. Schematic drawing of *SS* precursors beneath a hotspot location. The global map below shows the 17 hotspots included in this study and the binning windows containing *SS* reflection points.

2 DATA AND METHOD

Our data set consists of 13 years (from 1989 to 2001) of $M_w > 5.5$ earthquake records reported by Global Digital Seismic Network (GDSN), Mediterranean Network (MEDNET) and several other permanent and temporary regional deployments. A subset containing ~10 per cent of this database was analyzed in a recent study of the mantle structure beneath the northern Pacific Ocean (An *et al.* 2007). For the present study, we restrict the source-station distance range to 100–160° and group the selected source–receiver pairs according to their midpoint locations into 10° radius, spherical data gathers that centre on the 17 hotspots (see Gu *et al.* 2003 for details). We filter the resulting SH-component seismograms using corner frequencies of 0.02 Hz (low) and 0.08 Hz (high) and eliminate records that have signal-to-noise ratio (Gu *et al.* 1998) less than 5. The remaining number of quality records exceeds 70 for each hotspot, and the densest coverage is obtained in western North America and South Pacific Superswell (Fig. 1b).

We apply HRT, a slight variation of the least-squares Radon transform (LSRT) method outlined in An *et al.* (2007), to map the seismic data to a surrogate domain where individual waveforms can be easily isolated, classified, filtered and enhanced. For a suite of N seismograms denoted by $d(t, x_k)$, $k = 1, \ldots, N$, a noise-free Radon transformation (Hampson 1986) via an inverse formulation (Sacchi & Ulrych 1995; An *et al.* 2007; Gu & Sacchi 2009) can be expressed as

$$d(\tau, \Delta) = \sum_{j=1}^{M} r(\tau = t - p_j \Delta_i, p_j), \quad i = 1, \ldots, N, \tag{1}$$

where Δ_i represents the source–receiver distance of the ith seismogram, p_j represents the ray parameter for the jth arrival, and t and τ denote unreduced and reduced times relative to *SS*, respectively. We transform $d(\tau, \Delta)$ into the Fourier domain and apply the delay theorem (Papoulis 1962)

$$D(\omega, \Delta_k) = \sum_{j=1}^{M} R(\omega, p_j) e^{-i\omega\Delta_k p_j}, \tag{2}$$

where ω is an angular frequency, $R(\omega, p_j)$ is the Fourier transform of the time-domain Radon image and Δ_k represent the kth distance move-out from a reference value Δ_0 chosen between 100 and 160°. This summation can be rewritten as a linear equation using matrix notations

$$\mathbf{D}(\omega) = \mathbf{A}(\omega)\, \mathbf{R}(\omega), \tag{3}$$

where $\mathbf{A}(\omega)$ is a sensitivity matrix containing entries in the form of $e^{-i\omega\Delta_k p_j}$. The unknown vector $\mathbf{R}$ can be determined using linear inversions for all possible residual ray parameters p_j relative to that of *SS*. Eq. (3) can be solved by minimizing the following cost function:

$$J = ||\mathbf{D}(\omega) - \mathbf{A}(\omega)\mathbf{R}(\omega)||_2^2 + \mu \sum_{j}^{M} \ln(1 + a r_j)^2. \tag{4}$$

The first term on the right-hand side represents the data misfit, a measure of how well the forward Radon operator can reconstruct the data. The second term applies regularization (also known as penalty) to stabilize the solution. The difference between this formulation and the LSRT method is that the regularization term is now weighed by a sparseness constraint based on a Cauchy distribution (Sacchi & Ulrych 1995; Escalante *et al.* 2007). This weighting matrix can improve the resolution and phase identification in the Radon domain.

The final solution is determined by minimizing eq. (4) with respect to the unknown solution vector **R** (ω). The same equation must be solved for all angular frequencies ω to recover the full Radon operator $r(\tau, p_j)$ through an inverse Fourier transform. Figs 2(a and b) show a record section of partially stacked PREM synthetics, computed by summing the Earth's free oscillations in response to earthquake sources (Gilbert 1970), and the corresponding Radon solution. We measure τ–p (used interchangeably with 'Radon') values of *S410S* and *S660S* in distinct phase windows to accommodate different mantle shear velocity corrections. The depth of a given reflector is determined from the relative positions of the observed Radon peaks to those of PREM (Dziewonski & Anderson 1981; see also Gu & Sacchi 2009) synthetics. The reconstructed time series based on inverse Radon transform properly recovers the main phases of interest (Fig. 2c) and minimizes interfering arrivals such as core phases and top-side mantle reflections (Fig. 2d).

Under ideal data density and quality the τ–p solution for a coherent time-domain signal can be accurately determined by slowness slant-stacking (e.g. Gossler & Kind 1996), LSRT (An *et al.* 2007) or HRT method (this study). The main difference among these three methods is resolution, especially in ray parameter space (Fig. 3). Owing to Cauchy-based reweighting strategy (Escalante *et al.* 2007), the HRT method enhances the sparseness of the dominant Radon-domain signal (see Fig. 3) and produces higher-resolution, potentially more accurate, reconstructed time series than the LSRT approach. The choice of regularization could have a considerable effect on the accuracy of time and slowness measurements when the data constraint is less than ideal (see Gu & Sacchi 2009).

3 RADON IMAGING RESULTS

Fig. 4 shows a selection of waveforms and the corresponding Radon solutions beneath Hawaii and Iceland. Slight time adjustments have been applied to each trace to account for crustal thickness (Bassin *et al.* 2000), surface topography (ETOPO5) and mantle heterogeneity (Su *et al.* 1994). We pre-condition the data further by introducing a partial (20° wide) summation window to increase the clarity of traveltime move-outs prior to Radon inversions. The partially stacked time series show coherent peaks corresponding to reflections from the *410* and *660*, as well as modest signals potentially originated from other mantle depths (see Hawaii hotspot, Fig. 4).

We choose different minimum distance cut-offs (120° for Hawaii and 100° for Iceland) to improve the clarity of the *410* Radon peak(s) for accurate depth determinations. This subjective choice was prompted by a sharp change (or "bending") of *S410S* ray parameters at a source–receiver distance of ∼120° in several time-domain record sections (Gu & An 2007). The discontinuous *S410S* move-out curves present a challenge for reflector depth determination at a number of hotspots including Hawaii. For simplicity this study mainly concentrates on the dominant trend at distances >115° and omit the details on 2-D forward modelling of discontinuous traveltime curves (Gu & An 2007; Gu & Sacchi 2009).

Mantle reflectivity structures differ substantially beneath the 17 hotspots. The most problematic time-domain signals are observed beneath Afar (Fig. 5) where neither *S410S* nor *S660S* follows a coherent traveltime curve across the distance range of interest. The highly segmented *S410S* embodies the largest overall reflection amplitudes at most distances, but its inconsistent arrival times severely degrade the Radon solutions that are predicated on the

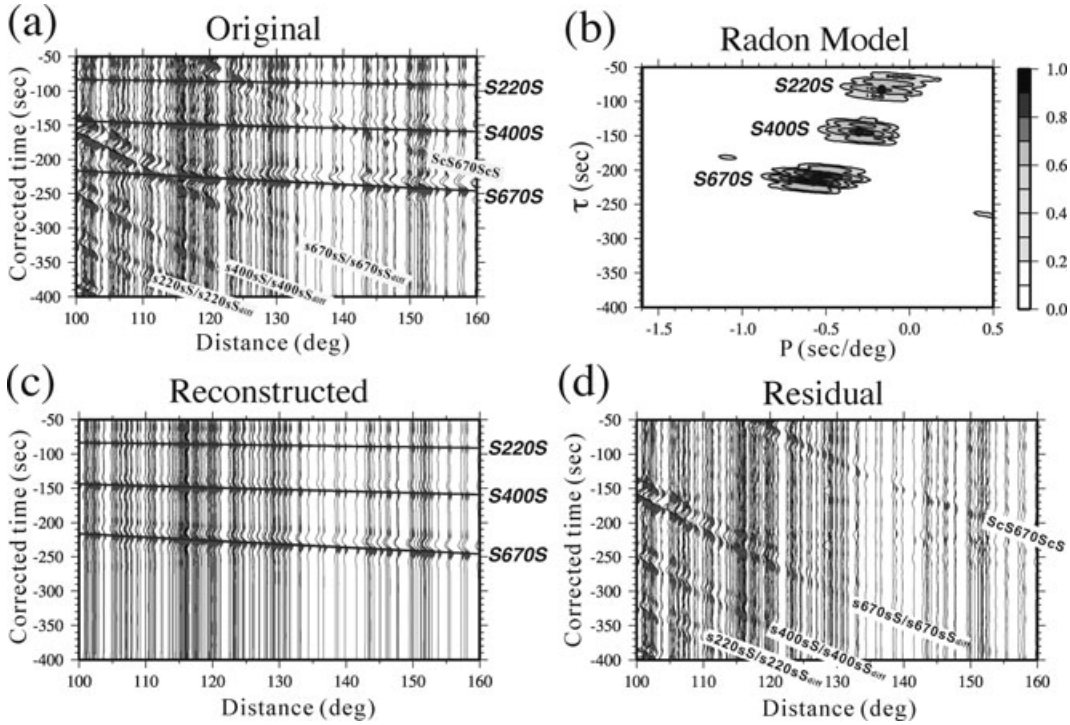

Figure 2. (a) PREM synthetic seismograms computed based on sample source–receiver pairs. These traces have been partially stacked (using a running average window of 20°) to enhance the signal-to-noise ratio. (b) Radon model obtained from the HRT method. The energy peaks result from underside reflections at 220-, 400- and 670-km depths. The contour lines mark the normalized amplitudes of 0.2, 0.4, 0.6 and 0.8; the maximum amplitude of the entire solution is set to 1. (c) Reconstructed time series based on the inverted Radon model. The main phases of interest are accurately predicted by the Radon solution. (d) Residual time series after subtracting the time series shown by (c) from (a). Both correlated (multiples) and random noise has been effectively eliminated.

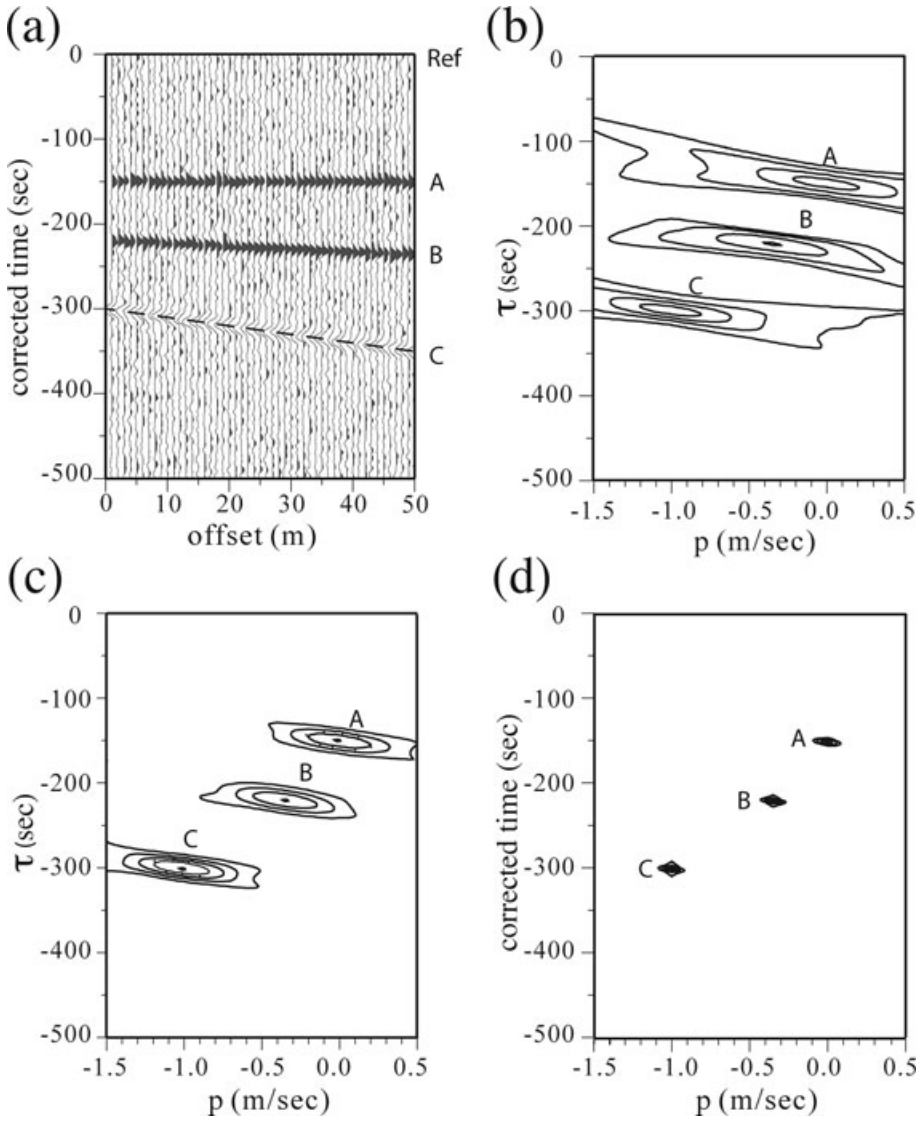

Figure 3. A synthetic data set containing 5 per cent random noise and three distinct peaks; phase C has a negative polarity. All traces are generated by the same velocity structure, source depth and focal mechanism. For simplicity, the input values (τ, p) of Radon peaks are (-150, 0), (-220, 0.35) and (-300, -1). Radon solutions based on (b) forward (Vespa), (b) LSRT and (c) HRT methods. The Radon amplitude in each case has been normalized by the maximum value of all three phases and the contour lines surrounding each $\tau - p$ signal denote the amplitude values of 0.2, 0.4, 0.6 and 0.8. Under idealized conditions all three methods produce equally accurate Radon maxima, but the HRT method improves the $\tau - p$ solutions substantially over the other two approaches.

smoothness of traveltime curves (see Fig. 5, middle left panel). In comparison, *S660S* traveltimes exhibit greater linearity both in the input and the reconstructed (and interpolated) time series (see Fig. 5, bottom panel), but the diminished reflection amplitudes away from the distance range of 120–140° remain problematic for an accurate determination of discontinuity depth.

3.1 Major MTZ discontinuities

The majority of hotspots show more robust Radon signals than Afar (Figs 6 and 7). We determine the depth of a given reflector from the time and ray parameter perturbations between the observed and predicted (based on PREM) Radon peak (Gu & Sacchi 2009). The inclusion of measured ray parameter in the calculation of reflector depth (e.g. Dziewonski & Gilbert 1976) is a key improvement over the conventional approach that assumes constant ray parameter from PREM (e.g. Gu *et al.* 2003). We estimate the measurement errors by the standard deviations of τ and p values using an automated Radon-domain bootstrapping method (An *et al.* 2007), and use reconstructed time series to assist error assessment further (Table 1).

S410S is the strongest reflection beneath hotspots. Its corresponding Radon-domain signals are nearly 50 per cent more energetic than that of *S660S*—the second strongest signal, under the Iceland (see Fig. 4), Azores (see Fig. 6), Macdonald, and Samoa (see Fig. 7) hotspots. The average depth of the *410* from 17 hotspots (from here on, the hotspot average) is 417 km, which is 7–8 km deeper than the global averages of 410 km (Gu *et al.* 2003; Deuss07) and 409 km (Houser *et al.* 2008) estimated using similar long-period data sets. Led by Hawaii and south Pacific Superswell, the *410* is especially deep at hotspots in the oceans (Fig. 8a). The general pattern is supported by the time-domain estimates of Deuss07 (Fig. 8b), as suggested by an overall correlation of 0.6. The large depression of the *410* beneath Hawaii is the most surprising result, considering

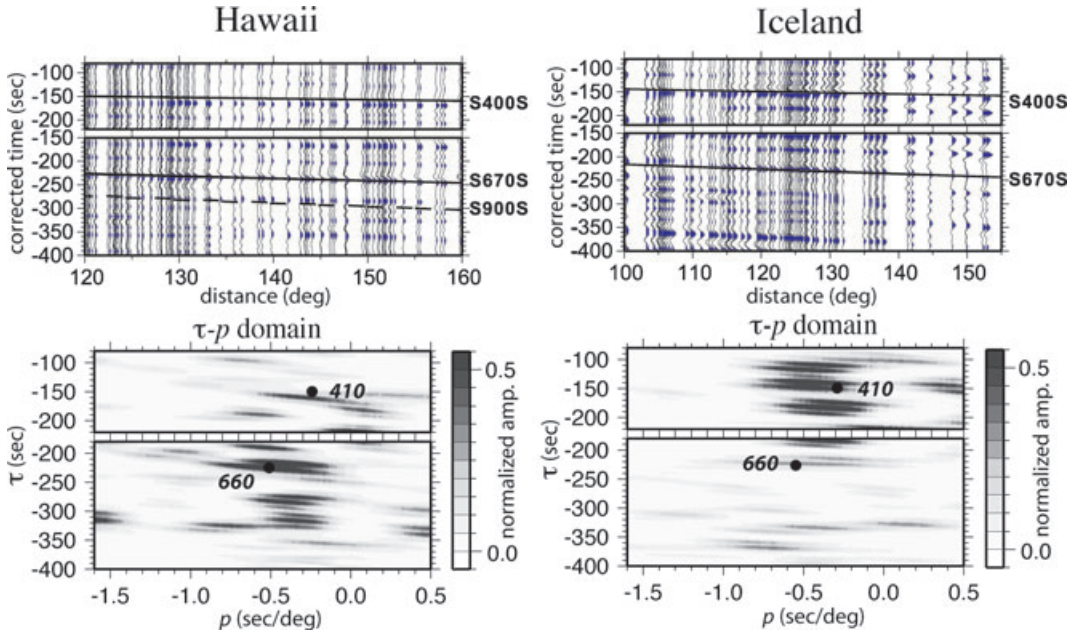

Figure 4. Sample time series and the corresponding Radon images for two hotspots. *S410S* and *S660S* are clearly identifiable in both time and Radon domains. The solid black circles denote the measured maximum τ and p locations from the corresponding synthetic seismograms. The letter '*L*' denotes to a lithospheric reflector for all plots from here on (Lehmann 1959). Various other Radon peaks are evidence of potential reflectors away from the MTZ.

that the previously published depths using SS precursors (e.g. Flanagan & Shearer 1998; Gu *et al.* 2003; Deuss07) are nearly identical to the global average. Some of the depth differences among the various studies can be attributed to differences in data density, selection criteria and/or midpoint gather positions. For example, earlier time-domain measurements in Flanagan & Shearer (1998) or Gu *et al.* (2003) were made based on 'cap' centres that do not coincide with the hotspot positions. Improved inversion/modelling strategies of this study also play a significant role since (1) true (rather than reference) ray parameters are used in our calculation of reflector depths, and (2) inversions for τ–p models utilize variable distance windows depending on the linearity of the *SS* precursor traveltime curves. An in-depth analysis of the latter effect is provided by Gu & Sacchi (2009).

The average depth of the *660* (653.4 km) is ∼4 km larger than the reported global average of 649 km using a similar data set (Gu *et al.* 2003). We identify substantial depressions under the Reunion and Hawaii hotspots and elevations under Afar and New England. The depths of the *410* and *660* exhibit similar trends beneath Pacific hotspots but show no visible global correlation (Fig. 8c). Excluding Hawaii (the largest outlier), the correlation between our measurements and those of Deuss07 is approximately 0.85 (Fig. 8d). Measurements pertaining to Pacific hotspots show the best agreement (to within 2 km) between these two studies. Of the two most notable outliers, the depth of the *660* under Reunion Island is questionable due to a diminished Radon peak, but a deep *660* beneath Hawaii is well constrained and would require a physical explanation.

3.2 Placing the hotspot mantle in a global framework

Similarities among hotspots can be just as revealing as the differences between them in the context of global characterization. First, a depressed *410* is supported by regionalized 'hotspot averages' computed from Gu *et al.* (2003) and Deuss07 (Fig. 9a) based on similar data constraints. The vast majority of the hotspots fall on the deeper side of the global average for three different studies shown in Fig. 9a. Second, the MTZ beneath 16 out of 17 hotspots is narrower than the reported global averages of 240–243 km (Fig. 9b) (Flanagan & Shearer 1998; Gu *et al.* 1998, 2003; Lawrence & Shearer 2006; Houser *et al.* 2008). The reduction of MTZ thickness is supported by recent observations from receiver functions (Lawrence & Shearer 2006) and *SS* precursors (Deuss07) beneath all but one hotspot. The lone exception to the general trends in *410* depth and MTZ thickness is Iceland, where the *410* is merely 407-km deep and the MTZ is 5–7 km thicker than the global average (see Fig. 8).

The *410* shows larger peak-to-peak depth variation than the *660* (Fig. 9c), and therefore, has greater impact on MTZ thickness. We do not observe a statistically significant correlation between the depths of the *410* and *660* beneath hotspots. Although de-correlation has been documented on the global scale (Flanagan & Shearer 1998; Gu *et al.* 1998, 2003), observations pertaining to hotspots (e.g. Gilbert *et al.* 2002; Fee & Dueker 2004; Du *et al.* 2006; Deuss 2007; this study) are potentially more meaningful considering the high temperatures (hence greater expected effect on mineral phase boundaries) associated with mantle plumes.

The main characteristics of the MTZ beneath hotspots are summarized in a statistical comparison with results from several published studies in Fig. 9(d). To differentiate the 'hotspot mantle' from the average oceanic mantle, we divide the Earth's mantle based on the tectonic regionalization scheme of Jordan (1981) and compare the median depths of the *410* under hotspots to the global and ocean averages. The average depths of the *410* beneath oceans do not systematically deviate from the global average (see Fig. 9d). However, the median *410* depths beneath hotspots are consistently deeper than the two larger-scale averages, especially in the two most recent studies where hotspots are carefully targeted (Deuss07) and potentially better resolved (this study). Deep *410* and thin MTZ beneath hotspots are accompanied by observations of low shear velocities in the upper mantle. According to model PR5 of Montelli *et al.* (2004), the upper mantle beneath the hotspots is, on

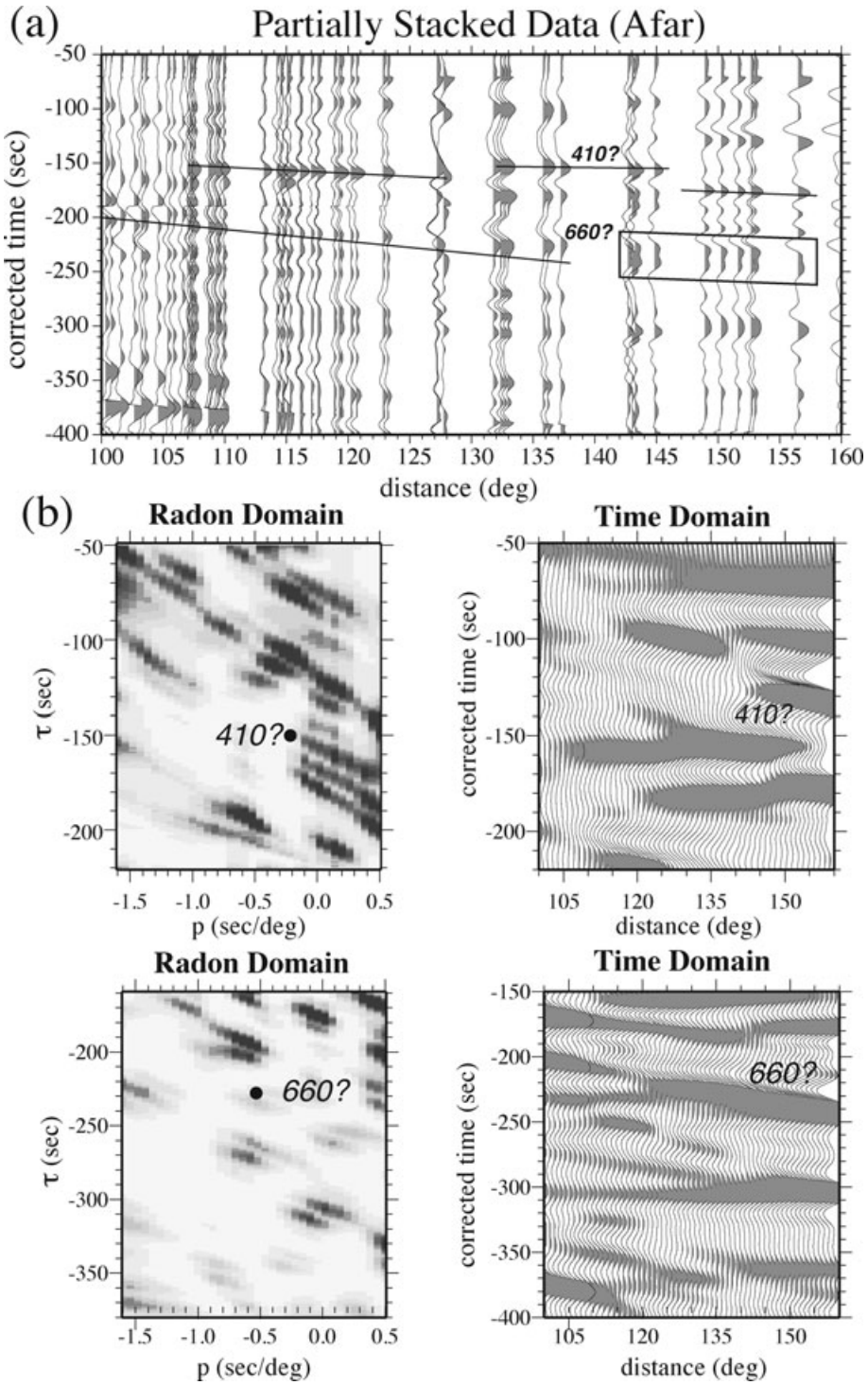

Figure 5. Time series and the corresponding Radon transform of the Afar hotspot. (a) The reflections (top panel) resulting from the *410* and *660* are strongly segmented and complex. The lines highlight the detectable phases within the data window. Waveforms contained in the box (142–156°) show the diminished *S660S* and, possibility, multiple arrivals. (b) Radon transform of the time series (left column, middle and bottom). The solid black circles mark the reference MTZ reflector positions (at 400 and 670 km, respectively) of PREM synthetic seismograms. Both *S410S* and *S660S* are missing from the Radon solution. The reconstructed time series (right column, middle and bottom) show substantial variations signal arrival times.

average, 1 per cent slower than beneath the "normal" oceanic lithosphere (see Fig. 9d). In other words, the anomalous traveltimes of *SS* precursors beneath hotspots are likely part of the cause, rather than the by-product, of previously reported continent-ocean differences (Gossler & Kind 1996; Gu *et al.* 1998) at the top of the MTZ.

The estimated discontinuity depths are, to varying degrees, influenced by the timing corrections for upper mantle heterogeneity. To verify the robustness of our observations, we re-compute the depth of the *410* using velocity corrections from eight published shear-velocity models (Fig. 10). Our calculations show that, despite

Table 1. Tabulated measurements from 17 hotspots.

Hotspot	Num. of Traces	Location		S670S				S400S				MTZ				
				τ (s)		*p* (s deg^{-1})		τ (s)		*p* (s deg^{-1})		400 km (km)		670 km (km)		Thickness (km)
		lat	long	syn	data	syn	data	syn	data	syn	data	Depth	Error	Depth	Error	
Afar	78	10	43	−226.16	−215.68	−0.515	−0.528	−149.09	−156.10	−0.273	−0.057	414	3.80	630	3.80	216
Azores	74	39	−28	−226.82	−221.79	−0.547	−0.635	−148.81	−154.58	−0.332	−0.173	420	0.58	646	1.17	226
Bowie	298	53	−135	−227.48	−223.42	−0.506	−0.498	−150.08	−156.05	−0.283	−0.387	411	1.28	652	0.66	241
Canary	89	28	−20	−227.22	−220.58	−0.517	−0.585	−151.18	−155.71	−0.253	−0.252	412	1.01	645	1.11	233
Cape Verde	63	14	−20	−227.57	−224.32	−0.514	−0.485	−150.17	−155.40	−0.287	−0.130	414	2.30	650	2.82	236
Hawaii	224	20	−156	−227.23	−224.72	−0.519	−0.498	−149.89	−160.44	−0.268	−0.260	436	2.20	672	2.96	236
Iceland	110	65	−20	−226.72	−225.44	−0.548	−0.155	−149.50	−151.54	−0.290	−0.182	407	1.49	655	2.10	248
Juan de Fuca	195	46	−130	−227.96	−223.00	−0.515	−0.610	−150.96	−160.13	−0.243	−0.214	420	2.46	653	2.34	233
Louisville	112	−51	−141	−227.82	−228.04	−0.516	−0.343	−151.17	−155.18	−0.243	−0.275	421	3.37	657	2.56	236
Macdonald	180	−30	−140	−227.70	−225.29	−0.531	−0.603	−150.89	−156.80	−0.218	−0.085	418	1.59	654	2.77	236
Marqueses	176	−10	−138	−226.80	−224.38	−0.533	−0.517	−149.47	−157.32	−0.285	−0.392	421	1.62	652	2.48	231
New England	98	28	−32	−226.45	−221.83	−0.568	−0.437	−149.97	−156.74	−0.269	−0.175	422	1.68	653	0.70	231
Pitcairn	155	−26	−130	−227.48	−227.46	−0.516	−0.620	−149.87	−155.29	−0.291	−0.317	416	1.31	654	2.87	238
Reunion	114	−21	56	−227.30	−227.24	−0.498	−0.478	−150.02	−156.94	−0.250	−0.320	419	2.12	659	2.38	240
Samoa	110	−14	−170	−226.44	−223.65	−0.532	−0.673	−149.44	−154.71	−0.269	−0.357	414	1.01	650	1.32	236
Tahiti	301	−18	−150	−227.07	−223.84	−0.536	−0.599	−149.69	−158.34	−0.288	−0.198	421	2.31	657	2.16	236
Yellowstone	155	44	249	−227.86	−221.13	−0.534	−0.708	−150.02	−157.43	−0.274	0.078	413	3.40	655	1.10	242
mean	145											417.6		652.6		235.0

considerable changes in the standard deviations of depth distribution—most notably the case of saw24b16 (Megnin & Romanowicz 2000), the average discontinuity depth remains 7–8 km deeper than the global average of ∼410 km. The median, which is a more resistant measure to large outliers, mainly falls in the range of 415–420 km.

3.3 Other reflectors

Potential reflections from the lithosphere and seismic velocity structures at 500–600, 800–920 and 1000–1100 km depths are frequently identified on the Radon images (see Figs 5–7). These seismic arrivals were previously difficult to quantify due to weak reflection amplitudes and interference from side-lobes of larger phases (Shearer 1993; Neele *et al.* 1997; Schmerr & Garnero 2006). The HRT method largely overcomes such observational limitations by simultaneously constraining ray parameters (through windowing in Radon domain) and time. Reflections from lithosphere depths, which arrive at 80–120 s prior to *SS*, are the most consistent signals apart from the two major MTZ reflections (Fig. 11). Their arrival times are regionally variable, as reflections from most oceanic hotspots, especially in the southern Pacific Ocean, arrive closer to the surface reflection than hotspots in and near continents (e.g. Yellowstone, Cape Verde). In comparison, signatures from a potential *520* are only reliably identified beneath hotspots in the northern Atlantic Ocean (e.g. Iceland, Azores, Cape Verde, and Canary hotspots) (see Fig. 11). The limited visibility of the *520* (<30 per cent) among the examined hotspots is inconsistent with earlier reports of their global (Shearer 1991) or oceanic (Gu *et al.* 1998; Deuss & Woodhouse 2001) presence. The hotspot – ocean difference will be discussed further in Section 4.

The presence of shallow lower-mantle reflectors is documented by seismic phases arriving 220–300 s before *SS*. The amplitude and depth of these reflectors are highly variable and their spatial distribution shows no particular affinity to the oceans (see Fig. 11). The Radon peaks associated with these potential reflectors are, in some cases, far from the respective values predicted by PREM. Although this observation raises questions on the nature of these late arriving phases, it should also be recognized that significant perturbations of reflection angle (hence, ray parameter) can be caused by dipping interfaces and/or the presence of 3-D mantle heterogeneities. A full 3-D analysis and simulation of *SdS* waveforms will be needed to accurately quantify these arrivals. The observed time- and Radon-domain signals 300 s away from *SS* remain a mystery. As indicated by the Yellowstone and Cape Verde hotspots (see Fig. 6), these arrivals can have unusually large amplitudes and/or anomalous ray parameters.

4 DISCUSSIONS

The HRT method provides simultaneous constraints on the timing, velocity and ray parameter of the *SS* precursors. The nominal lateral resolution of the data is 1000–1500 km, which is larger than the typical dimension of a 'primary' hotspot (e.g. Courtillot *et al.* 2003; Steinberger & Antretter 2006). Wave front healing (Montelli *et al.* 2004) and a complex *SdS* Fresnel zone (Shearer 1993; Neele *et al.* 1997) present further challenges to plume imaging. On the other hand, the combination of heat dissipation and plume ponding (or tilting) at the base of the *660* (e.g. Ebinger & Sleep 1998; Ritsema *et al.* 1999; Shen *et al.* 2002; Manglik & Christensen 2006; Nolet *et al.* 2006) or lithosphere (Anderson 2005) can potentially improve the visibility of hot thermal anomalies. The main observations and

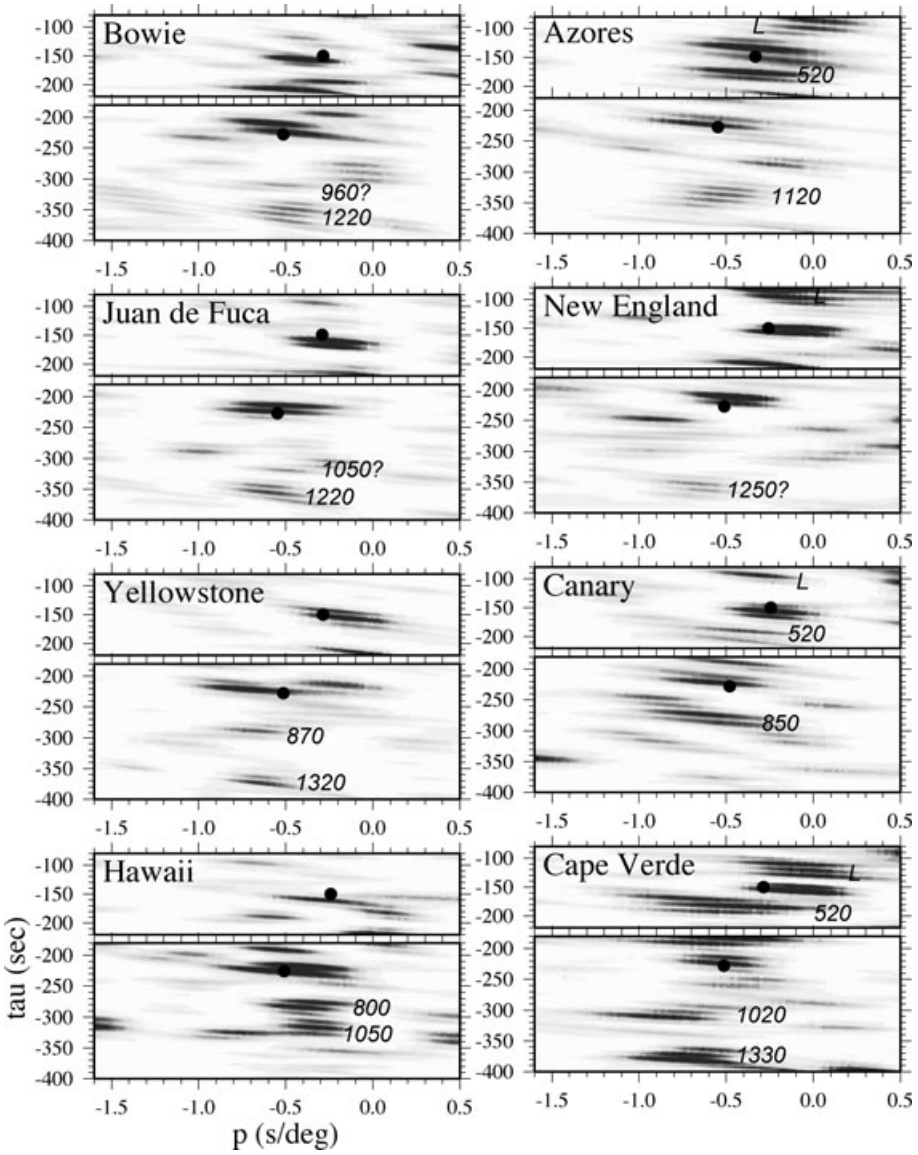

Figure 6. The radon image of eight hotspots in the Northern Hemisphere. The solid black circles mark the positions of measured MTZ peaks from PREM synthetic seismograms. The difference between observed and predicted Radon peaks reflect structural and dip differences (see main text). Most of these Radon images show robust energy peaks preceding the MTZ phases. Some of these signals are potentially caused by lower mantle reflectors at the depths that are indicated on the plot.

conclusions are summarized by a schematic sketch (Fig. 12) and discussed in the following sections.

4.1 Upper mantle and the *410*

The Radon images highlight the *410* as one of the most effective plume trackers beneath hotspots (see also Deuss07; Tauzin *et al.* 2008). Our study shows an average depression of 7–8 km relative to IASP91 model (Kennet 1991) (see Fig. 8) beneath hotspots which, assuming a Clapeyron slope of +2.9 MPa K^{-1} (Bina & Helfrich 1994; Presnall 1995) for the solid–solid phase transition from olivine to wadsleyite (Walker & Agee 1989; Katsura & Ito 1989), translates to a temperature increase of 70–120 K relative to the global average near the top of the MTZ. Observations of regionally depressed *410* are not limited to lateral length scales larger than 1000 km, the nominal resolution of *SS* precursors. For instance, depressions on the order of 10–15 km have recently been reported based on higher-resolution (at length scales <500 km) *P*-to-*S* converted waves (Tauzin *et al.* 2008). The moderate depth difference between these two length scales can be readily accounted for by heat dissipation and the effect of averaging. The continuity and shape of the inferred upper mantle thermal anomaly are not firmly established by the topography on the *410*, however. Due to imperfect shear velocity model corrections, an isolated low-velocity body near the *410* (which predominantly influences *S410S* times) and a distributed hot thermal anomaly above the *410* (which dictates the *SS* times) can cause similar traveltime differences between *SS* and *S410S*. In other words, the aforementioned 70–120 K temperature estimate should be interpreted as the upper bound of thermal variations since the *SS*-*S410S* traveltime residuals are preferentially mapped to phase boundary perturbations (see Fig. 12). Still, the presence of low-velocity anomalies with a minimum diameter of 1000 km appears to be a common link between *SS* precursor observations and results of traveltime/waveform tomography (e.g. Ritsema *et al.* 1999;

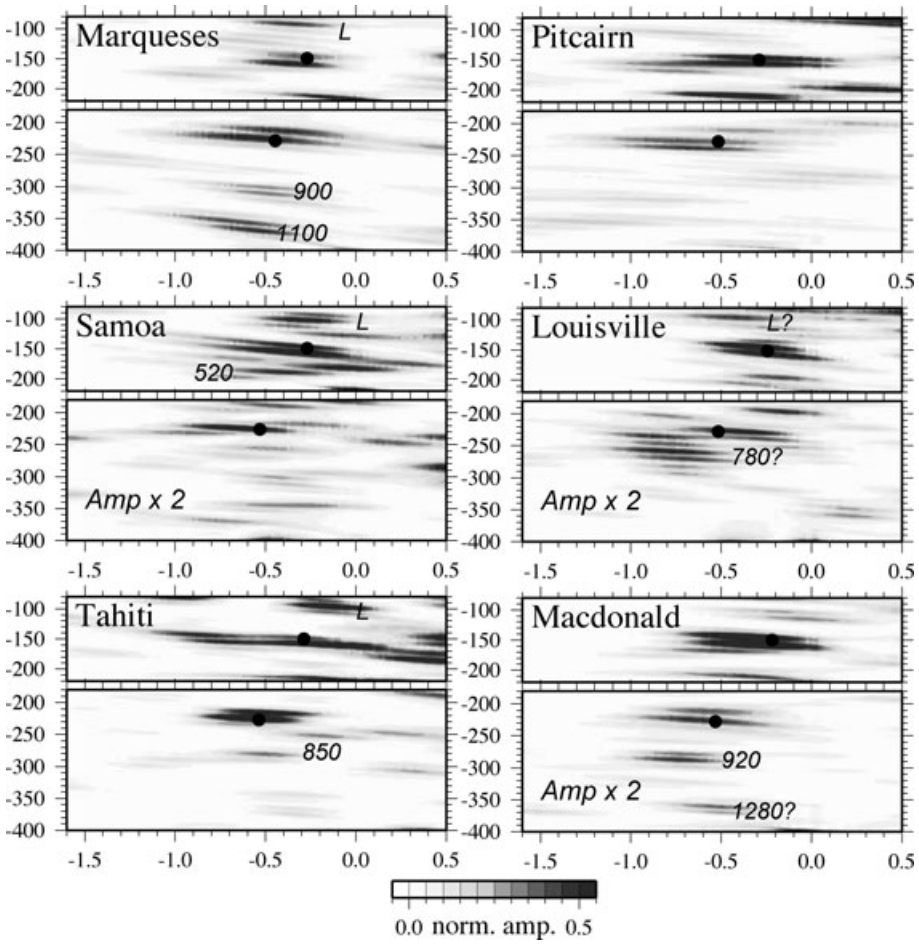

Figure 7. Radon image of six hotspots in the Southern Hemisphere. The plot conventions are the same as Fig. 6.

Megnin & Romanowicz 2000; Gu *et al.* 2001; Montelli *et al.* 2004; Hung *et al.* 2004; Zhao 2004; Nolet *et al.* 2006).

Strong reflections off the *410* offer further evidence for a hot thermal structure in the upper mantle beneath hotspots. It has been suggested that the phase loop of olivine to wadsleyite transition (Helffrich & Bina 1994) is temperature-dependent and directly impacts the sharpness of the *410* reflection. A hypothesized positive correlation between reflection amplitude and temperature based on thermodynamic considerations (e.g. Bina & Helffrich 1994) is supported by observations of a diffuse/missing *410* phase boundary beneath subduction zones (Flanagan & Shearer 1999) and a sharp boundary beneath high-temperature regions (Benz & Vidale 1993). Hence, despite lateral variations in discontinuity depth (or, mantle temperature), increased sharpness due to a relatively warm upper mantle can provide a simple explanation for the enhanced *410* amplitudes beneath the majority of the hotspots.

In addition to temperature, the presence of water (Hellfrich & Wood 1996; Ito *et al.* 1999; Bercovici & Karato 2003), partial melt (Revenaugh & Sipkin 1994) and compositional heterogeneities (Anderson 1989; Nolet & Ziehuis 1994; Frost 2003) may also lower the *410* and affect the amplitudes of bottom-side shear wave reflections. For example, the presence of wet, enriched residue in the 'global water filter' model (Bercovici & Karato 2003) on top of the MTZ (Karato & Jung 1998) can potentially reduce the speed of *S410S* and increase the impedance contrast at ∼410 km. However, with this filtration process being sufficiently suppressed for mantle plumes (Bercovici & Karato 2003), the dehydration-induced melting process should have greater overall impact on the global average than on the hotspot average. The net result will reduce, rather than amplify, the overall depth difference of the *410* between hotspot and the average mantle.

Localized silicate melt (Revenaugh & Sipkin 1994) or hydrated wadsleyite 'lens' (Schmerr & Garnero 2007) can also have similar effects as temperature on the properties of the *410*, especially near subduction zones. The drawback of this class of models is that the 'wetness' of mantle plumes—a key parameter and catalyst in the initiation of partial melting, is still debated beneath global hotspots and oceans (e.g. Hirth & Kohlstedt 1996; Ito *et al.* 1999; Dixon & Clague 2001; Jamtveit *et al.* 2001; Nichols *et al.* 2002; Hirschmann 2006; Silveira *et al.* 2006; also see Yoshino *et al.* 2008 for interpretations of laboratory conductivity experiments). Other compositional variations such as Fe enrichment through plume entrainment (Javoy 1999) or garnet transition (Thybo *et al.* 2003) can influence the MTZ by broadening the olivine phase loop, but both mechanisms will reduce the visibility of the *410* and therefore conflict with the observed high reflection amplitudes beneath hotspots. In short, a warm upper mantle remains the simplest, if not the most viable, explanation for a deep and sharp *410* interface beneath the global hotspots.

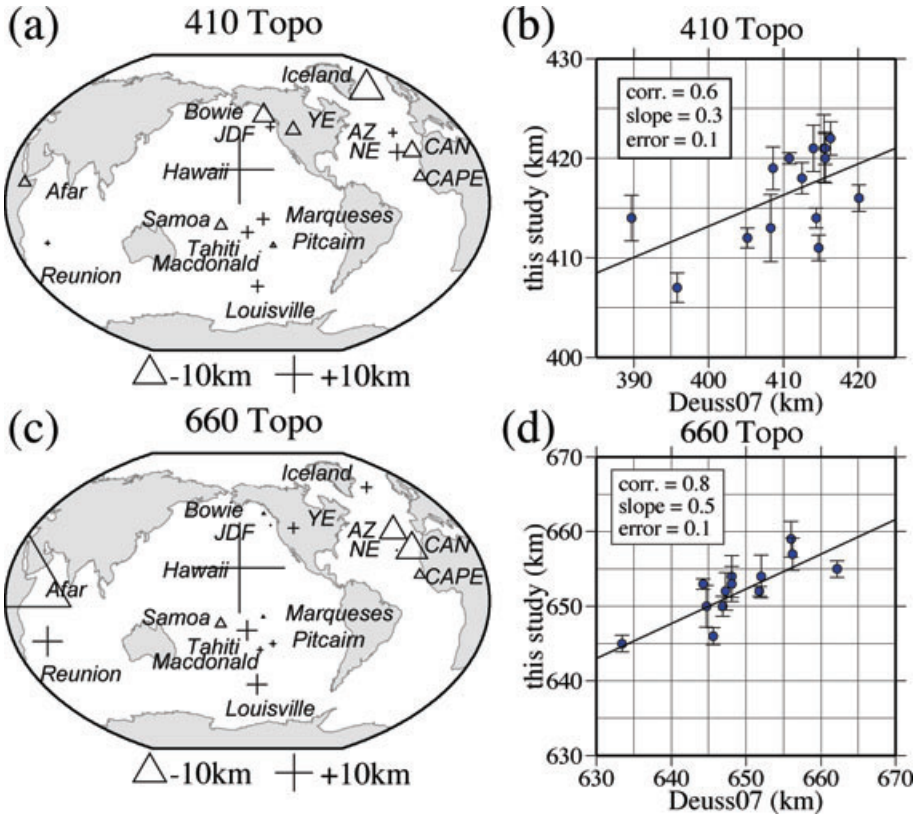

Figure 8. Depth perturbations of the *410* and *660* and their correlation with the respective measurements from Deuss 2007. (a) Depth perturbation of the *410* relative to the average (417 km) from all 17 hotspots. (b) Depth correlation of the *410*. Independently determined depths are available at 14 hotspots. (c) Depth perturbation of the 660 relative to the average (653 km) from all 17 hotspots. (d) Similar to (b), but for the *660* (a total of 13 hotspots were examined by both studies).

4.2 MTZ and the *660*

MTZ thickness estimates are routinely invoked to determine the existence and vertical continuity of thermal anomalies. In an isochemical Pyrolite mantle (Ringwood 1975) dominated by two olivine phase transitions of opposite Clapeyron slopes (Katsura & Ito 1989; Ito & Takahashi 1989), a thin MTZ would be expected from converging phase boundaries in response to uninterupted vertical upwelling (e.g. Gu & Dziewonski 2002; Niu *et al.* 2002; Lawrence & Shearer 2006; Deuss07). However, the effectiveness of MTZ thickness as a vertical plume tracker can be compromised by uncorrelated topography on the *410* and *660* (as in this study) or major complexities within MTZ (e.g. mid-MTZ velocity reversals and multiple mineral phase boundaries) (Vinnik & Fara 2006; Deuss &Woodhouse 2002; Saikia *et al.* 2008; Tauzin *et al.* 2008). Separate discussions of the internal MTZ structure and the characteristics of the *660* will be needed.

First, our study shows that the internal structure of the MTZ under the majority of the hotspots is surprisingly 'uneventful'. Often coined as a global seismic discontinuity (Revenaugh & Jordan 1991; Shearer 1990, 1991, 1996; Flanagan & Shearer 1998), a mid-MTZ reflector at ∼520-km depth has been widely documented in oceanic regions (e.g. Gu *et al.* 1998; Gao *et al.* 2002) and less frequently observed beneath continents (Ryberg *et al.* 1997). Earlier studies attributed its origin to an exothermic phase transition from wadsleyite to ringwoodite (e.g. Ito & Takahashi 1989; Shearer 1990; Ita & Stixrude 1992), but recent evidence from seismology (Deuss & Woodhouse 2002) and mineral physics (Saikia *et al.* 2008) suggested multiple phase boundaries involving both olivine (at ∼520 km) and garnet (at ∼560 km) may be responsible. The Radon-domain signal between *S410S* and *S660S* is nearly 'white' beneath hotspots, which is inconsistent with the average *S520S* amplitude (3–5 per cent to SS; Gu *et al.* 1998; An *et al.* 2007) beneath oceanic regions. We hypothesize that the sharpness and magnitude(s) of wadsleyite to ringwoodite and/or garnet to perovskite transition (1) decrease with increased temperature (Xu *et al.* 2008) and (2) may be affected by compositional variations due to variable fertility of the mantle and the proportion of recycled oceanic crust (Saikia *et al.* 2008). Based on the above assumptions, weak or missing reflections from 500 to 600 km depth (as shown in Figs 5–7) would imply that the MTZ portion of the 'hotspot mantle' is warmer than, and potentially compositionally distinct from, the average oceanic mantle.

Second, the mantle structure at the base of MTZ appears to be more complex than the structure within it. Our observations of a relatively flat but deeper-than-average *660* cannot be easily explained by the ringwoodite to silicate perovskite + magnesiowüstite transformation under high mantle temperatures. The lack of a negative correlation between topography and temperature signals either average mantle temperatures surrounding the *660* (e.g. Gilbert *et al.* 2003; Du *et al.* 2006) or strong interference from other mantle processes or mineralogy (e.g. Weidner & Wang 1998; Hirose 2002; Deuss07; Tauzin *et al.* 2008). The former explanation favours the decoupling of a warm upper mantle (see Section 4.1) from an average/colder-than-average lower mantle beneath a

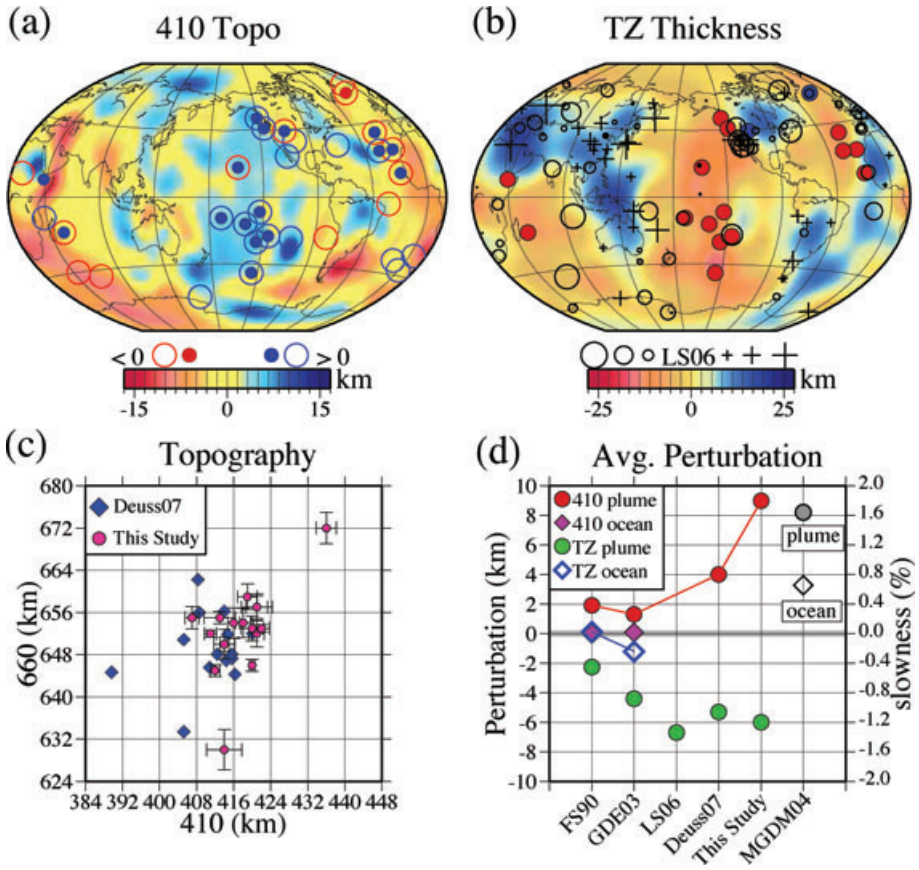

Figure 9. (a) Depth perturbations relative to the global average of 410 km. The background colour map shows the measurements of Gu *et al.* (2003). Solid circles represent the results of this study (only polarity is plotted against the global average) and the large unfilled circles show the corresponding results of Deuss07. (b) Transition zone thickness perturbations relative to the global average of 242 km (based on past studies using *SS* precursors). The background colour map shows the interpolated thickness measurements of Gu & Dziewonski (2002). The foreground unfilled circles and crosses represent thin and thick MTZ, respectively, from Lawrence & Shearer (2006). The solid circles show the results from this study. (c) Correlation (or the lack of) between the depths of *410* and *660* for both this study and Deuss07. The uncertainties of our measurements are as indicated. (d) A statistical analysis of hotspot and ocean averages from various studies. In all cases the *410* is deeper and the MTZ is thinner under hotspots than under oceans. The black symbols show the slowness (reciprocal of velocity, see right-hand axis labels) perturbations predicted by Montelli *et al.* (2004) shear velocity model.

number of the hotspots (e.g. Nolet *et al.* 2006), which implies that these hotspots initiate within or above the MTZ. Alternatively, the exothermic phase change from majorite to perovskite (e.g. Weidner & Wang 1998, 2000; Hirose 2002) could overlap with the ringwoodite to perovskite phase loop under high temperatures (Hirose 2002). Consequently, the '*660*' we report here may reflect a relatively broad, 'grey area' (see Fig. 12) predicated on the temperature–pressure conditions and the stability of majorite (Hirose 2002). This hypothesis does not require a major temperature difference between the upper and lower mantle, and the considerable depressions of the *660* under the Reunion, Tahiti and Macdonald hotspots could originate from a dominating majorite to perovskite transformation within a hot, vertically continuous plume (e.g. Weidner & Wang 1998; Hirose 2002). For the same hotspots, a wide olivine phase loop (e.g. Bina & Helffrich 1994) at mantle temperatures of 2000+ K could become seismically undetectable.

4.3 Lithosphere and lower mantle

With the exceptions of the Hawaii and Yellowstone hotspots, the Radon images consistently show seismic reflections arriving 80–120 s prior to the *SS* (see Figs 5, 6 and 11). We refer to these signals as "*L*" reflections (Lehmann 1959), even though the actual depths of the reflectors fluctuate between 160 km (beneath Southern Pacific hotspots) and 300 km (beneath northern Atlantic hotspots). The global existence (Dziewonski & Anderson 1981) of seismic discontinuities between 150 and 350 km is still debated (Kennet 1991; Shearer 1993), despite reports of their presence beneath stable continents (Jordan 1975; Gaherty & Jordan 1995; Gu *et al.* 2001; Li *et al.* 2002; Deuss & Woodhouse 2002) and plate boundaries (Revenaugh & Jordan 1991; Vidale & Benz 1992; Bostock 1996; Gu *et al.* 2005). The presence of L reflections under the majority of the hotspots, especially in the central Atlantic Ocean (see Fig. 12), is at odds with the average signal from time-domain stacks of *SS* precursors beneath oceans (Shearer 1993; Gu *et al.* 2001; Deuss & Woodhouse 2002). In addition to well-documented mechanisms in connection with mantle rheology, anisotropy and potential phase change (e.g. Karato 1992; Gaherty & Jordan 1995; Gung *et al.* 2003; Deuss & Woodhouse 2004; William & Revenaugh 2005), tilted/ponded plume material as a consequence of plume-plate interaction (e.g. Ebinger & Sleep 1998; Farnetani *et al.* 2002; Shen *et al.* 2002; Manglik & Christensen 2006; Nolet *et al.* 2006) could play a key role in shaping the upper mantle reflectivity structure beneath hotspots. For instance, lateral expansion of

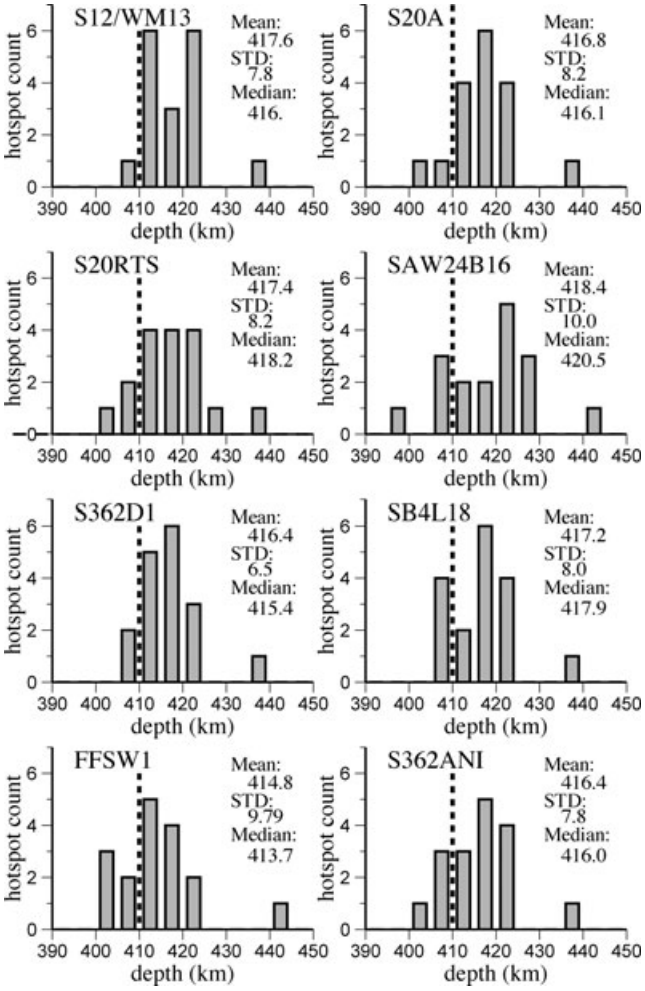

Figure 10. Distributions of the depth of the *410* after applying heterogeneity corrections based on S12 (Su *et al.* 1994), S20A (Ekström & Dziewonski 1998), saw24b16 (Megnin & Romanowicz 2000), S20RTS (Ritsema *et al.* 1999), S362D1 (Gu *et al.* 2001), SB4L18 (Masters *et al.* 2000), FFSW1 (Zhou *et al.* 2006) and S362ANI (Kustowski *et al.* 2008). VSH is used in the calculation of corrections for anisotropic models S20A, FFSW1 and S362ANI. Despite considerable differences among the distributions, the average discontinuity depth remains nearly constant at a value close to 417 km.

plume head along lower-plate interface can increase plume visibility and form a low-velocity (and possibly molten) layer (e.g. Farnetani *et al.* 2002; Manglik & Christensen 2006) from trapped plume material. Consequently, the combined plate and plume-layer thickness and the bottom-side impedance contrast will dictate (and delay) the reflection time beneath both continents and oceans; the slow-to-fast transition will induce a positive reflection amplitude. This hypothesis is supported by the presence of deep *L* reflectors in the vicinity of the western African mobile belt (250–300 km) and consistently shallow ones in the southern and central Pacific Ocean (160–220 km) (see Figs 11 and 12).

In addition, our Radon images identify a series of deep reflectors in the depth range of 800–1300 km beneath Hawaii, Louisville, Tahiti, Juan de Fuca, Canary and Macdonald Islands (see Figs 5–7). Similar reflecting structures have been previously reported near active subduction zones (Niu & Kawakatsu 1997; Deuss & Woodhouse 2001; Niu *et al.* 2003; Vanacore *et al.* 2006; Rost *et al.* 2008; Courtier & Revenaugh 2008) and attributed to (1) mechanical/chemical segregation caused by stagnant slab in the lower mantle (e.g. Niu *et al.* 2003; Vanacore *et al.* 2006) and (2) phase transitions in metastable garnet (Kubo *et al.* 2002) or in hydrous magnesium/aluminium-bearing silicates (Ohtani *et al.* 1995; Shieh *et al.* 1998; Lakshtanov *et al.* 2007; Courtier & Revenaugh 2008). These mechanisms are generally unsuitable for the observed mid-mantle reflectors away from convergent plate boundaries (e.g. Le Stunff *et al.* 1995; Shen *et al.* 2003; An *et al.* 2007) due to their requisite pressure-temperature conditions and dependency on cold/water-rich slabs in the lower mantle. Alternative suggestions of a global mid-mantle chemical boundary layer (Wen & Anderson 1997; Shen *et al.* 2003) should be carefully considered, especially for relatively 'quiet' regions such as northeastern Pacific Ocean (An *et al.* 2007). Verification of these mechanisms requires a true global survey based on improved data constraints and higher-resolution imaging methods such as Radon transforms (An *et al.* 2007; this study) and migration (e.g. see review by Rost & Thomas 2009). Still, in the absence of a true global reflectivity map, the mere presence of mid-mantle reflectors beneath hotspots is a strong indication that the chemistry and thermodynamics at mid-mantle depths are more complex than those suggested by the spectral content of seismic velocities (e.g. Megnin & Romanowicz 2000; Gu *et al.* 2001; Becker & Boschi 2002).

5 CONCLUSIONS

The most important property of HRT is its ability to differentiate consistent phase arrivals (as Radon peaks) from spurious ones that coincidentally occur within the time window of interest. By using the HRT approach, we are able to confidently resolve the existence, depth and strength of multiple mantle reflectors beneath 17 major hotspot locations (seeFig. 12). We observe that

1. *S*-wave reflections from the *410* are the highest amplitude Radon signals beneath hotspots.
2. The *410* beneath hotspots is 7–9 km deeper than the global average, suggesting that the upper mantle/MTZ beneath hotspots is 70–120 K warmer than the average mantle.
3. The MTZ beneath the hotspots is 5–7 km thinner than the global average.
4. Reflections from the *660* are weak (relative to those from the *410*) and the inferred ∼3 km positive variation relative to the global average suggests that, in addition to olivine phase transitions, Majorite garnet to Perovskite transition may play a critical role near the bottom of the upper mantle under high temperature conditions.
5. Reflections from the *520* are rarely observed, possibly due to the broadening of the wadsleyite to ringwoodite phase transition under high MTZ temperatures.
6. The L discontinuity and a series of lower mantle reflectors exist under hotspots.

Although the observations presented in this study do not necessarily reveal the exact origin and depth of mantle plumes, they do underscore the *existence* and *effects* of large-scale thermal anomalies down to MTZ depths beneath the majority of the hotspots. The wide-ranging observations convey a simple message: the temperature and stratigraphy of the upper mantle and MTZ beneath hotspots are most likely *different* from the average oceanic mantle.

ACKNOWLEDGMENTS

We sincerely thank Gillian Foulger and Adam Dziewonski for insightful scientific discussions. We also thank Arwen Deuss

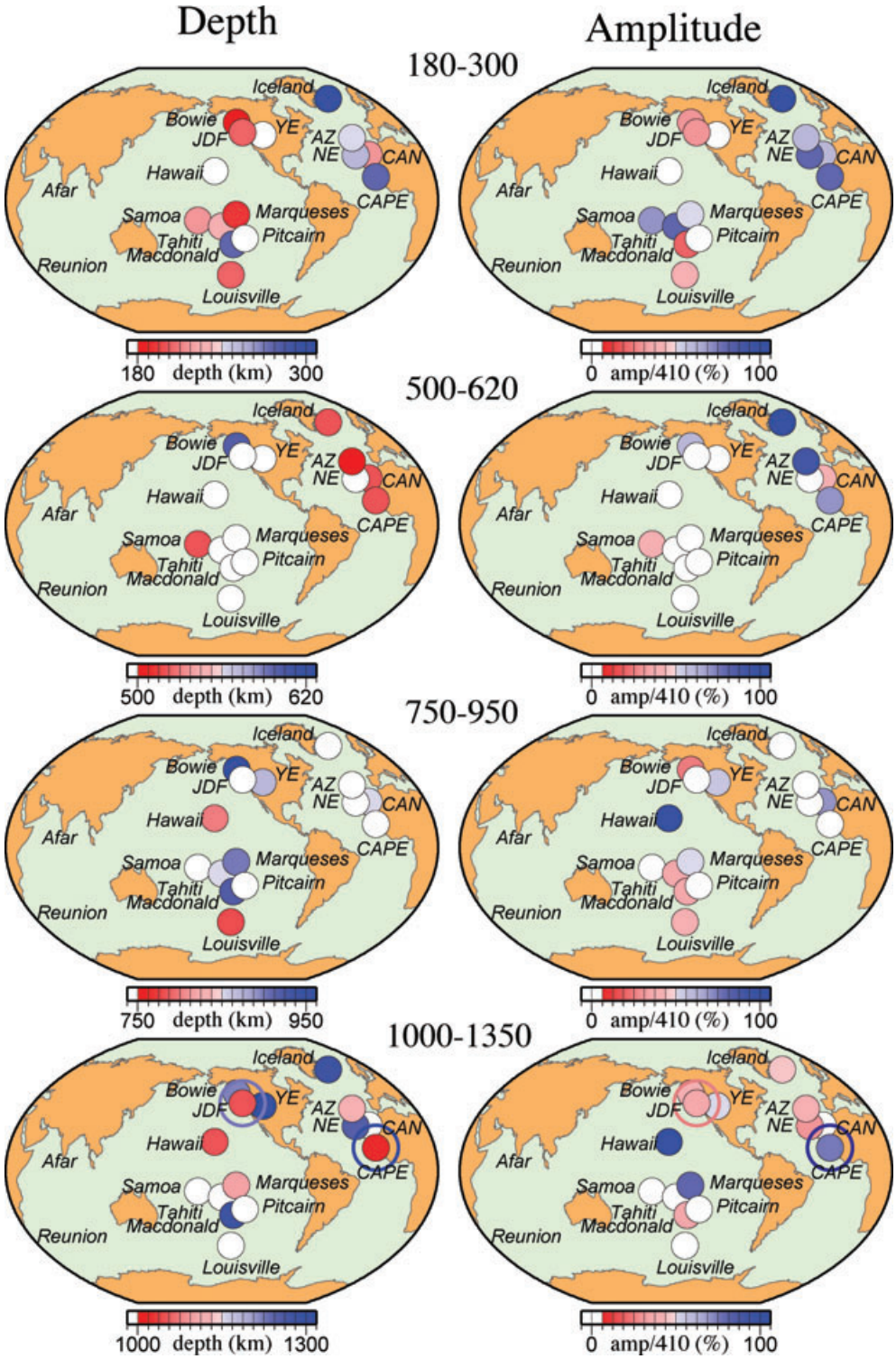

Figure 11. Depth and impedance contrast of various mantle reflectors. For a given reflection, the amplitude (right column) corresponds to the percentage Radon amplitude ratio between a reflection and *S410S*; the latter phase is the strongest signal in this study. The large unfilled circles in the bottom-row maps (labelled '1000–1350') indicate the presence of a second reflector and their colours follow the same convention as the solid circles.

and an anonymous reviewer for their constructive suggestions and comments. Much of the work presented here was based on the MSc thesis of Yuling An (currently at CCGVeritas) and an undergraduate summer project conducted by Ryan Schultz. We also thank IRIS for data archiving and dissemination. Some of the figures presented were prepared using the GMT software (Wessel & Smith 1995). The research project is funded by Alberta Ingenuity, National Science and Engineering Council (NSERC) and Canadian Foundation for Innovations (CFI).

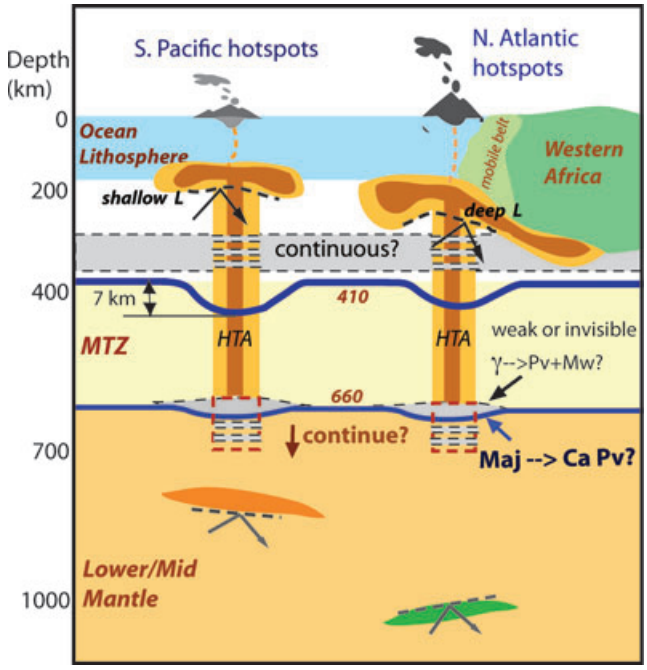

Figure 12. A schematic drawing of the main observations and interpretations of this study. The strength of a given reflector is documented by the thickness of the lines; for example, the *410* is represented by a stronger colour and a thicker line than the *660*. The abbreviations are: Ca Pv (Ca perovskite), Maj (Majorite garnet), HTA (hot thermal anomaly), γ (ringwoodite), *L* (lithospheric reflector), M_w (magnesiowustite), and Pv (perovskite). The lateral dimension of the HTA is assumed to be ~1000 km, which is not drawn in scale. The grey stripes denote regions where the presence or continuity of a hot plume is not well-resolved.

REFERENCES

Agee, C.B. & Walker, D., 1988. Olivine flotation in mantle melt, *Earth planet. Sci. Lett.,* **90,** 144–156.

An, Y., Gu, Y.J. & Sacchi, M., 2007. Imaging mantle discontinuities using least-squares Radon transform, *J. geophys. Res.,* **112,** doi:10.1029/2007JB005009.

Anderson, D.L., 1989. *Theory of the Earth,* Blackwell Scientific Publications, Oxford, UK, 388 pp.

Anderson, D.L., 2001. Top-Down Tectonics?, *Science,* **293,** 2016–2018.

Anderson, D.L., 2005. Scoring hot spots: the plume and plate paradigms, in *Plates, Plumes, and Paradigms,*Vol. 388, pp. 31–54, eds Foulger, G.R., Natland, J.H., Presnall, D.C. & Anderson, D.L., Geological Society of America.

Bassin, C., Laske, G. & Masters, M.G., 2000. The current limits of resolution for surface wave tomography in North America, *EOS Trans. Am. geophys. Un.,* **81,** Fall. Meet. Suppl., F897.

Becker, T.W. & Boschi, L., 2002. A comparison of tomographic and geodynamic mantle models, *Geochem., Geophys., Geosys.,* **3**(1), 1003, doi:10.1029/2001GC000168.

Benz, H.M. & Vidale, J.E., 1993. The sharpness of upper mantle discontinuities determined from high-frequency P′P′ precursors, *Nature,* **365,** 147–150.

Bercovici, D. & Karato, S.-J., 2003. Whole mantle convection and the transition-zone water filter, *Nature,* **425,** 39–44.

Bina, C.R. & Helffrich, G.R., 1994. Phase transition clapeyron slopes and transition zone seismic discontinuity topography, *J. geophys. Res.,* **99,** 15 853–15 860.

Bostock, N.G., 1996. Ps conversions from the upper mantle transition zone beneath the Canadian landmass, *J. geophys. Res.,* **101,** 8393–8402.

Courtillot, V., Davaillie, A., Besse, J. & Campbell, I.H., 2003. Three distinct types of hotspots in the Earth's mantle, *Earth Planet. Sci. Lett.,* **205,** 295–308.

Courtier, A.M. & Revenaugh, J., 2008. Slabs and shear wave reflectors in the midmantle, *J. geophys. Res.,* **113,** B08312, doi:10.1029/2007JB005261.

Davies, G.F., 1988. Ocean bathymetry and mantle convection, 1. Large-scale flow and hotspots, *J. geophys. Res.,* **93,** 10 467–10 480.

Deuss, A., 2007. Seismic observations of transition-zone discontinuities beneath hotspot locations, in *Plates, plumes and planetary processes,*Special Paper 430, pp. 121–136, eds Foulger, G.R. & Jurdy, D.M., Geological Society, doi:10.1130/2007.2430(07).

Deuss, A. & Woodhouse, J.H., 2001. Seismic observations of splitting of the mid-transition zone discontinuity in the Earth's mantle, *Science,* **294,** 354–357.

Deuss, A. & Woodhouse, J.H., 2002. A systematic search for mantle discontinuities using SS-precursors, *Geophys. Res. Lett.,* **29,** 1–4.

Deuss, A. & Woodhouse, J.H., 2004. The nature of the Lehmann discontinuity from its seismological Clapeyron slopes, *Earth planet. Sci. Lett.,* **225,** 295–304.

Dixon, J.E. & Clague, D.A., 2001. Volume of basaltic glasses from Loihi seamount, Hawaii: evidence for a relatively dry plume component, *J. Petrol.,* **42,** 627–654.

Du, Z., Vinnik, L.P. & Foulger, G.R., 2006. Evidence from *P*-to-*S* mantle converted waves for a flat '660-km' discontinuity beneath Iceland, *Earth planet. Sci. Lett.,* **241,** 271–280.

Dziewonski, A.M. & Anderson, D.L., 1981. Preliminary reference Earth model, *Phys. Earth planet. Inter.,* **25,** 297–356.

Dziewonski, A.M. & Gilbert, F., 1976. Effect of small, aspherical perturbations on travel times and re-examination of the corrections for ellipticity, *Geophys. J. R. astr. Soc.,* **44,** 7–16.

Ebinger, C.J. & Sleep, N.H., 1998. Cenozoic magmatism throughout east Africa resulting from impact of a single plume, *Nature,* **395,** 788–791.

Ekström, G. & Dziewonski, A.M., 1998. The unique anisotropy of the Pacific upper mantle, *Nature,* **394,** 168–172.

Escalante, C., Gu, Y.J. & Sacchi, M., 2007. Simultaneous iterative time-domain deconvolution to teleseismic receiver functions, *Geophys. J. Int.,* **171,** 316–325, doi:10.1111/j.1365–246x.2007.03511.x.

Farnetani, C.G., Bernard, L. & Tackley, P.J., 2002. Mixing and deformations in mantle plumes, *Earth planet. Sci. Lett.,* **196,** 1–15.

Fee, D. & Dueker, K., 2004. Mantle transition zone topography and structure beneath the Yellowstone hotspot, *Geophys. Res. Lett.,* **31,** L18603, doi:10.1029/2004GL020636.

Flanagan, M.P. & Shearer, P.M., 1998. Global mapping of topography on transition zone velocity discontinuities by stacking SS precursors, *J. geophys. Res.,* **103,** 2673–2692.

Flanagan, M.P. & Shearer, P.M., 1999. A map of topography on the 410-km discontinuity from PP precursors, *Geophys. Res. Lett.,* **26,** 549–552.

Foulger, G.R., 2007. The "plate" model for the genesis of melting anomalies,Vol. 430, pp. 1–28, *Geological Society of America* Special Paper **430,** 1–28.

Frost, D.J., 2003. The structure and sharpness of (Mg, Fe)$_2$SiO$_4$ phase transformations in the transition zone, *Earth planet. Sci. Lett.,* **216,** 313–328.

Fukao, Y., Widiyantoro, S. & Obayashi, M., 2001. Subduction slabs stagnant in the mantle transition zone, *J. geophys. Res.,* **97,** 4809–4822.

Gaherty, J.B. & Jordan, T.H., 1995. Lehmann discontinuity as the base of an anisotropic layer beneath continents, *Science,* **268,** 1468–1471.

Gao, S.S., Silver, P.G., Liu, K.H. & Kaapvaal Seismic Group, 2002. Mantle discontinuities beneath Southern Africa, *Geophys. Res. Lett.,* **29**(10), doi:10.1029/2001GL013834.

Gilbert, F., 1970. Excitation of the normal modes of the Earth by earthquake sources, *Geophys. J. R. astr. Soc.,* **22,** 223–226.

Gilbert, J.H., Sheehan, A.F., Dueker, K.G. & Molnar, P., 2003. Receiver functions in the western United States, with implications for upper mantle structure and dynamics, *J. geophys. Res.,* **108**(B5), 2229, doi:10.1029/2001JB001194.

Gossler, J. & Kind, R., 1996. Seismic evidence for very deep roots of continents, *Earth planet. Sci. Lett.,* **138,** 1–13.

Grand, S.P., Van Der Hilst, R.D. & Widiyantoro, S., 1997. Global seismic tomography: a snapshot of convection in the Earth, *GSA Today,* **7,** 1–7.

Gu, Y.J. & An, Y., 2007. Searching for mantle plumes using high-resolution Radon transforms, available at www.mantleplumes.org.

Gu, Y.J., Dziewonski, A.M. & Agee, C.B., 1998. Global de-correlation of the topography of transition zone discontinuities, *Earth planet. Sci. Lett.,* **157,** 57–67.

Gu, Y.J. & Dziewonski, A.M., 2002. Global variability of transition zone thickness, *J. geophys. Res.,* **107,** doi:10.1029/2001JB000489.

Gu, Y.J., Dziewonski, A.M. & Ekström, G., 2001. Preferential detection of the Lehmann discontinuity beneath continents, *Geophys. Res. Lett.,* **28,** 4655–4658.

Gu, Y.J., Dziewonski, A.M. & Ekström, G., 2003. Simultaneous inversion for mantle shear velocity and topography of transition zone discontinuities, *Geophys. J. Int.,* **154,** 559–583.

Gu, Y.J., Lerner-Lam, A., Dziewonski, A.M. & Ekström, G., 2005. Seismic evidence for deep anisotropy beneath the East Pacific Rise, *Earth planet. Sci. Lett.,* **232,** 259–272.

Gu, Y.J. & Sacchi, M., 2009. Radon transform methods and their applications in mapping mantle reflectivity structures, *Surv. Geophys.,* in press.

Gung, Y., Panning, M. & Romanowicz, B., 2003. Global anisotropy and the thickness of continents, *Nature,* **422,** 707–711.

Hampson, D., 1986. Inverse velocity stacking for multiple elimination, *J. Can. Soc. Expl. Geophys.,* **22**(1), 44–55.

Helffrich, G. & Bina, C., 1994. Frequency dependence of the visibility and depths of mantle seismic discontinuities, *Geophys. Res. Lett.,* **21,** 2613–2616.

Helffrich, G. & Wood, B., 1996. 410 km discontinuity sharpness and the form of the olivine-phase diagram: resolution of apparent seismic contradictions, *Geophys. J. Int.,* **126,** 7–12.

Hirose, K., 2002. Phase transitions in pyrolitic mantle around 670-km depth: implications for upwelling of plumes from the lower mantle, *J. geophys. Res.,* **107,** doi:10.1029/2001JB000595.

Hirschmann, M.M., 2006. Water, melting and the deep Earth H_2O cycle, *Ann. Rev. Earth Planet. Sci.,* **34,** 629–653.

Hirth, G. & Kohlstedt, D.L., 1996. Water in the oceanic upper mantle; implications for rheology, melt extraction and the evolution of the lithosphere, *Earth planet. Sci Lett.,* **144,** 93–108.

Houser, C., Masters, G., Flanagan, M. & Shearer, P.M., 2008. Determination and analysis of long-wavelength transition zone structure using SS precursors, *Geophys. J. Int.,* **174,** 178–194, doi:10.111/j.1365–246X.2008.03719.x.

Hung, S.H., Shen, Y. & Chiao, L.Y., 2004. Imaging seismic structure beneath the Iceland hotspot: A finite frequency approach, *J. geophys. Res.,* **109,** B08305, doi:10.1029/2003JB002889.

Ita, J.J. & Stixrude, L., 1992. Petrology, elasticity and composition of the transition zone, *J. geophys. Res.,* **97,** 6849–6866.

Ito, E. & Takahashi, E., 1989. Postspinel transformations in the system Mg_2SiO_4–Fe_2SiO_4 and some geophysical implications, *J. geophys. Res.,* **94,** 10 637–10 646.

Ito, G., Shen, Y., Hirth, G. & Wolfe, C.J., 1999. Mantle flow, melting, and dehydration of the Iceland mantle plume, *Earth planet. Sci. Lett.,* **165,** 81–96.

Jamtveit, B., Brooker, R., Brooks, K., Melchior Larsen, L. & Pedersen, T., 2001. The water content of olivine from the North Atlantic Volcanic Province, *Earth planet. Sci. Lett.,* **186,** 401–415.

Javoy, M., 1999. Chemical Earth models, *C. R. Acad. Sci. Paris,* **329,** 537–555.

Jordan, T.H., 1975. The continental lithosphere, *Rev. Geophys. Space Phys.,* **13,** 1–12.

Jordan, T.H., 1981. Global tectonic regionalization for seismological data analysis, *Bull. Seismol. Soc. Am.,* **71,** 1131–1141.

Karato, S.-I., 1992. On the Lehmann discontinuity, *Geophys. Res. Lett.,* **19,** 2555–2558.

Karato, S.-I. & Jung, H., 1998. Water, partial melting and the origin of the seismic low velocity and high attenuation zone in the upper mantle, *Earth planet. Sci. Lett.,* **157,** 193–207.

Katsura, T. & Ito, E., 1989. The system Mg_2SiO_4–Fe_2SiO_4 at high pressures and temperatures; precise determination of stabilities of olivine, modified spinel, and spinel, *J. geophys. Res.,* **94,** 15 663–15 670.

Kellogg, L.H., Hager, B.H. & Van Der Hilst, R.D., 1999. Compositional stratification in the deep mantle, *Science,* **283,** 1881–1884, doi:10.1126/science.283.5409.1881.

Kennett, B.L.N. (Compiler and Editor), 1991. *IASPEI 1991 Seismological Tables,* Bibliotech, Canberra, Australia, 167 pp.

Kovlenko, V.I., Naumov, V.B., Girnis, A.V., Dorofeeva, V.A. & Yarmolvuk, V.V., 2006. Composition and chemical structure of oceanic mantle plumes, *Petrology,* 452–476, doi:10.1134/S0869591106050031.

Kubo, T. *et al*. 2002. Metastable garnet in oceanic crust at the top of the lower mantle, *Nature,* **420,** 803–806.

Kustowski, B., Ekström, G. & Dziewoński, A.M., 2008. Anisotropic shear-wave velocity structure of the Earth's mantle: a global model, *J. geophys. Res.,* **113,** B06306, doi:10.1029/2007JB005169.

Lakshtanov, D. *et al*. 2007. The post-stishovite phase transition in hydrous aliuminum-bearing SiO_2 in the lower mantle of the Earth, *Proc. Nat. Acad. Sci.,* **104,** 13 588–13 590.

Lay, T., 2005. The deep mantle thermal-chemical boundary layer: the putative mantle plume source, *Geological Society of America,* Special Paper 388. 188–205.

Le Stunff, Y., Wicks, C.W. Jr. & Romanowicz, B., 1995. P′P′ precursors under Africa: evidence for mid-mantle reflectors, *Science,* **270,** 74–77.

Lawrence, J.F. & Shearer, P.M., 2006. A global study of transition zone thickness using receiver functions, *J. geophys. Res.,* **111,** doi:10.1029/2005JB003973.

Lehmann, I., 1959. Velocities of longitudinal waves in the upper part of the Earth's mantle, *Geophys. J. R. astr. Soc.,* **15,** 93–113.

Li, A., Fischer, K.M., Van Der Lee, S. & Wysession, M., 2002. Crust and upper mantle discontinuity structure beneath eastern North America, *J. geophys. Res.,* **107,** doi:10.1029/2001JB000190.

Li, X., Kind, R., Priestley, K., Sobolev, S.V., Tilmann, F., Yuan, X. & Weber, M., 2000. Mapping the Hawaiian plume conduit with converted seismic waves, *Nature,* **427,** 827–829.

Lin, S.-C., Kuo, B.-Y., Chiao, L.-Y. & van Keken, P.E., 2005. Thermal plume models and melt generation in East Africa: a dynamic modeling approach, *Earth planet. Sci. Lett.,* **237,** 175–192.

Manglik, A. & Christensen, U.R., 2006. Effect of lithospheric root on decompression melting in plume-lithosphere interaction models, *Geophys. J. Int.,* **164,** 259–270.

Masters, G., Laske, G., Bolton, H. & Dziewonski, A., 2000. The relative behavior of shear velocity, bulk sound speed, and compressional velocity in the mantle: implications for chemical and thermal structure, *AGU Monogr. ser. 'Seismol. Miner. Phys.',* **117,** 63–87.

Megnin, C. & Romanowicz, B., 2000. The 3-D shear velocity structure of the mantle from the version of body, surface and high mode waveforms, *Geophys. J. Int.,* **143,** 709–728.

Montelli, R., Nolet, G., Dahlen, F.A., Masters, G., Engdah, E.R. & Hung, S.H., 2004. Finite-frequency tomography reveals a variety of plumes in the mantle, *Science,* **303,** 338–343.

Morgan, W.J., 1971. Convection plumes in the lower mantle, *Nature,* **230,** 42–43.

Nataf, H.-C., 2000. Seismic imaging of mantle plumes, *Annu. Rev. Earth planet Sci.,* **28,** 391–417.

Neele, F., de Regt, H. & Van Decar, J., 1997. Gross errors in upper-mantle discontinuity topography from underside reflection data, *Geophys. J. Int.,* **129,** 194–204.

Nichols, A.R., Carroll, M.R. & Hoskuldsson, A., 2002. Is the Iceland hotspot also wet? Evidence from submarine and subglacial pillow basalts, *Earth planet. Sci. Lett.,* **202,** doi:10.1016/S0012–821X(02)00758-6.

Niu, F. & Kawakatsu, H., 1997. Depth variation of the mid-mantle seismic discontinuity, *Geophys. Res. Lett.,* **24**(4), 429–432.

Niu, F., Solomon, S.C., Silver, P.G., Suetsugu, D. & Inoue, H., 2002. Mantle transition-zone structure beneath the South Pacific Superswell and evidence for a mantle plume underlying the Society hotspot, *Earth planet. Sci. Lett.,* **198,** 371–380.

Niu, F., Kawakatsu, H. & Fukao, Y., 2003. Seismic evidence for a chemical heterogeneity in the midmantle: a strong and slightly dipping seismic reflector beneath the Mariana subduction zone, *J. geophys. Res.,* **108**(B9), 2419, doi:10.1029/2002JB002384.

Nolet, G. & Ziehuis, A., 1994. Low S velocities under the Tornquist-Teisseyre zone: evidence for water injection into the transition zone by subduction. *J. geophys. Res.,* **99,** 15813–15820.

Nolet, G., Karato, S.-I. & Montelli, R., 2006. Plume fluxes from seismic tomography, *Earth planet. Sci. Lett.,* **248,** 685–699.

Ohtani, E., Shibata, T., Kubo, T. & Kato, T., 1995. Stability of hydrous phases in the transition zone and the upper most part of the lower mantle, *Geophys. Res. Lett.,* **22,** 2553–2556.

Panning, M. & Romanowicz, B., 2006. A three-dimensional radially anisotropic shear velocity in the whole mantle, *Geophys. J. Int.,* **167,** 361–379.

Papoulis, A., 1962. *The Fourier Integral and its Applications,* McGraw-Hill, New York.

Presnall, D.C., 1995. Phase diagrams of Earth-forming minerals, in *Mineral Physics and Crystallography: A Handbook of Physical Constants,* Am. geophys. Un., Washington, DC.

Revenaugh, J. & Jordan, T.H., 1991. Mantle Layering From *ScS* Reverberations 3. The Upper Mantle, *J. geophys. Res.,* **96,** 19781–19810.

Revenaugh, J. & Sipkin, S.A., 1994. Seismic evidence for silicate melt atop the 410-km mantle discontinuity, *Nature,* **369,** 474–476.

Ringwood, A.E., 1975. *Composition and Petrology of the Earth's Mantle,* McGraw-Hill, 630 pp.

Ritsema, J., Van Heijst, H.J. & Woodhouse, J.H., 1999. Complex shear wave velocity structure imaged beneath Africa and Iceland, *Science,* **286,** 1925–1928.

Ritsema, J.H., van Heijst, J. & Woodhouse, J.H., 2004. Global transition zone tomography, *J. geophys. Res.,* **109,** doi:10.1029/2003JB002610.

Romanowicz, B., 2003. Global mantle tomography: progress status in the last 10 years, *Annu. Rev. Geophys. Space Phys,* **31,** 303–328.

Rost, S., Garnero, E.J., William, Q. & Manga, M., 2005. Seismological constraints on a possible plume root at the core-mantle boundary, *Nature,* **435,** 666–669.

Rost, S., Garnero, E.J. & Wiliam, Q., 2008. Seismic array detection of subducted oceanic crust in the lower mantle, *J. geophys. Res.,* **113,** B06303, doi:10.1029/2007JB005263.

Rost, S. & Thomas, C., 2009. Improving seismic resolution through array processing techniques, *Surv. Geophys.,* in press.

Ryberg, T., Wenzel, F., Egorkin, A.V. & Solodilov, L., 1997. Short-period observation of the 520 km discontinuity in northern Eurasia, *J. geophys. Res.* **102,** 5413–5422.

Sacchi, M. & Ulrych, T.J., 1995. High-resolution velocity gathers and offset space reconstruction, *Geophysics,* **60,** 1169–1177.

Saikia, A., Frost, D. & Rubie, D., 2008. Splitting of the 520-kilometer seismic discontinuity and chemical heterogeneity in the mantle, *Science,* **319,** 1515–1518.

Schmerr, N. & Garnero, E.J., 2006. Investigation of upper mantle discontinuity structure beneath the central Pacific using SS precursors, *J. geophys. Res.,* doi:10.1029/2005JB004197.

Schmerr, N. & Garnero, E.J., 2007. Upper mantle discontinuity topography from thermal and chemical heterogeneity, *Science,* **318,** 623–626.

Shearer, P.M., 1990. Seismic imaging of upper-mantle structure with new evidence for a 520-km discontinuity, *Nature,* **344,** 121–126.

Shearer, P.M., 1991. Imaging global body-wave phases by stacking long-period seismograms, *J. geophys. Res.,* **96,** 20,353–20,364.

Shearer, P.M., 1993. Global mapping of upper mantle reflectors from long-period SS precursors, *Geophys. J. Int.,* **115,** 878–904.

Shearer, P.M., 1996. Transition zone velocity gradients and the 520-km discontinuity, *J. geophys. Res.,* **101,** 3053–3066.

Shen, Y. *et al*. 2002. Seismic evidence for a tilted mantle plume and north–south mantle flow beneath Iceland, *Earth planet. Sci. Lett.,* **197,** 262–272.

Shen, Y., Wolfe, C.J. & Solomon, S.C., 2003. Seismological evidence for a mid-mantle discontinuity beneath Hawaii and Iceland, *Earth planet. Sci. Lett.,* **214,** 143–151.

Shieh, S.R., Mao, H., Hemley, R.J. & Ming, L.C., 1998. Decomposition of phase D in the lower mantle and the fate of dense hydrous silicates in subducting slabs, *Earth planet. Sci. Lett.,* **159,** 13–23.

Silveira, G., Stutzmann, E., Davaille, A., Montagner, J.-P., Mendes-Victor, L. & Sebai, A., 2006. Azores hotspot signature in the upper mantle, *J. Volc. Geotherm. Res.,* **156,** doi:10.1016/j.jvolgeores.2006.03.022.

Sleep, N.H., 1990. Hotspots and mantle plumes: some phenomenology, *J. geophys. Res.,* **95,** 6715–6736.

Sleep, N.H., Einger, C.J. & Kendall, J.-M., 2002. Deflection of mantle plume material by cratonic keels, in *The Earth: Physical, Chemical and Biological Development,* 199, pp. 135–150, eds Fowler, C.M.R., Ebinger, C.J. & Hawkesworth, C.J., Geological Society of London Special Publication.

Steinberger, B., Sutherland, R. & O'Connell, R.J., 2004. Prediction of emperor-Hawaii seamount locations from a revised model of global plate motion and mantle flow, *Nature,* **430,** 167–173.

Steinberger, B. & Antretter, M., 2006. Conduit diameter and buoyant rising speed of mantle plumes: implications for the motion of hot spots and shape of plume conduits, *Geochem. Geophys. Geosyst.,* **7,** Q11018, doi:10.1029/2006GC001409.

Su, W.J., Woodward, R.L. & Dziewonski, A.M., 1994. Degree-12 model of shear velocity heterogeneity in the mantle. *J. geophys. Res.,* **99,** 6945–6980.

Tackley, P.J. Stevenson, D.J., Glatzmaier, G. & Schubert, G., 1993. Effects of an endothermic phase transition at 670-km in a spherical model of the convection in the Earth's mantle, *Nature,* **361,** 699–704.

Tauzin, B., Debayle, E. & Wittlinger, G., 2008. The mantle transition zone as seen by global Pds phases: no clear evidence for a thin transition zone beneath hotspots, *J. geophys. Res.,* **113,** B08309, doi:10.1029/2007JB005364.

Thybo, H., Nielsen, L. & Perchuc, E., 2003. Seismic scattering at the top of the mantle Transition Zone, *Earth planet. Sci Lett.,* **216,** 259–269.

Trampert, J. & van Heijst, H., 2002. Global azimuthal anisotropy in the transition zone, *Science,* **296,** 1297–1299.

Vanacore, E., Niu, F. & Kawakatsu, H., 2006. Observations of the mid-mantle discontinuity beneath Indonesia from *S* to *P* converted waveforms, *Geophys. Res. Lett.,* **33,** L04302, doi:10.1029/2005GL025106.

Van Der Hilst, R., Widiyantoro, S. & Engdahl, R., 1997. Evidence for deep mantle circulation from global tomography, *Nature,* **386,** 578–584.

Van Der Hilst, R.D. & Karason, H., 1999. Compositional heterogeneity in the bottom 1000 kilometers of Earth's mantle: toward a hybrid convection model, *Science,* **286,** 1925–1928.

Vidale, J.E. & Benz, H.M., 1992. Upper-mantle seismic discontinuities and the thermal structure of subduction zones, *Nature,* **356,** 678–683.

Vinnik, L. & Farra, V., 2006. Svelocity reversal in the mantle transition zone, *Geophys. Res. Lett.,* **33,** L18316, doi:10.1029/2006GL027120.

Visser, K., Trampert, J., Lebedev, S. & Kennet, B.L.N., 2008. Probability of radial anisotropy in the deep mantle, *Earth planet. Sci. Lett.,* **270,** 241–250.

Walker, D. & Agee, C., 1989. Partitioning 'equilibrium,' temperature gradients, and constraints on Earth differentiation, *Earth planet. Sci. Lett.,* **96,** 49–60.

Weidner, D.J. & Wang, Y., 1998. Chemical and Clapeyron-induced buoyancy at the 660 km discontinuity, *J. geophys. Res.,* **103,** 7431–7441.

Weidner, D.J. & Wang, Y., 2000. Phase transformations: implications for mantle structure, in *Earth Deep Interior: Mineral Physics and Tomography from the Atomic to the Global Scale* (*Geophys. Monogr. Ser.*),Vol. 117, pp. 215–235, eds Karato, S., Forte, A.M., Liebermann, R.C., Masters, G. & Stixrude, L., American Geophysical Union, Washington, DC.

Wessel, P. & Smith, W.H.F., 1995. The Generic Mapping Tools (GMT) version 3.0, *Technical Reference & Cookbook,* SOEST/NOAA

Williams, Q. & Revenaugh, J., 2005. Ancient subduction, mantle ecologite, and the 300 km seismic discontinuity, *Geology,* **33,** 1–4, doi:10.1130/G20968.1.

Wen, L. & Anderson, D., 1997. Layered mantle convection: a model for geoid and topography and seismology, *Earth Planet. Sci. Lett.,* **146,** 367–377.

Xu, W., Lithgow-Bertelloin, C., Stixrude, L. & Ritsema, J., 2008. The effect of bulk composition and temperature on mantle seismic structure, *Earth Planet. Sci. Lett.,* **275,** 70–79.

Yoshino, T., Manthilake, G., Matsuzaki, T. & Katsura, T., 2008. Dry mantle transition zone inferred from the conductivity of wadsleyite and ringwoodite, *Nature,* **451,** 326–329, doi:10.1038/nature06427.

Zhao, D., 2004. Global tomographic images of mantle plumes and subducting slabs: insight into deep Earth dynamics, *Phys. Earth Planet Int.,* **146,** 3–34.

Zhou, Y., Nolet, G., Dahlen, F.A. & Laske, G., 2006. Global upper-mantle structure from finite-frequency surface wave tomography, *J. geophys. Res.,* **111,** B04304, doi:10.1029/2005JB003677.